ARTICLE | Article in Press

HfB_2 and SiB_6 nanoparticles enhance heat-storage capacity, thermal conductivity, and thermal stability of $7NaNO_3$–$53KNO_3$–$40NaNO_2$ molten salt

Ezgi Gurgenc · Halil İbrahim Yamaç · Murat Özabacı · Canan Aksu Canbay · Turan Gurgenc · Muhammed Gür · Hakan F. Öztop · Elshan Sefidgar Shahanaghi

Received: 24 June 2026 / Accepted: 25 August 2026
© The Author(s) 2026

Abstract

Improving the heat-storage capacity, thermal conductivity, and high-temperature stability of nitrate–nitrite molten salts is essential for increasing the efficiency and operational reliability of concentrating solar power (CSP) systems. Accordingly, the effects of hafnium diboride (HfB_2) and silicon hexaboride (SiB_6) nanoparticles on the phase integrity, microstructural evolution, and thermophysical performance of $7NaNO_3$–$53KNO_3$–$40NaNO_2$ molten salt were comparatively investigated. Nanocomposite formulations containing 0.5-2 wt% additive were synthesized and characterized by XRD, FT-IR, FE-SEM/EDX, DSC, TGA, and TPS measurements. The results confirmed that nanoparticle incorporation did not disrupt the fundamental nitrate-nitrite salt framework, and no evidence of newly formed phases or chemical bond generation was identified. Despite this structural and chemical preservation, marked improvements were obtained in heat-storage and heat-transfer characteristics. The melting enthalpy increased from 76.2 J/g for the reference salt to 89.4–90.6 J/g in the HfB_2-containing compositions and to 92.6–95.6 J/g in the SiB_6-containing compositions. The highest specific heat capacity enhancement in the HfB_2 series occurred at 1.5 wt%, reaching 55.17% in the solid phase and 66.65% in the liquid phase, whereas the SiB_6 series exhibited its optimum response at 1 wt% with corresponding increases of 107.78% and 117.79%. Thermal conductivity rose from 0.951 W/m.K to 1.689 W/m.K with 2 wt% HfB_2 and 1.529 W/m.K with 2 wt% SiB_6. The degradation onset temperature also increased from 612 °C to 653 °C and 663 °C, respectively. These findings demonstrate that boride-based nanoadditives provide an effective route for improving the thermophysical performance and high-temperature durability of this molten salt, with HfB_2 delivering the strongest thermal conductivity enhancement and SiB_6 providing the most pronounced improvements in latent heat, specific heat capacity, and thermal stability.

Keywords Molten nitrate salt · Boride nanoparticles · Latent heat behavior · TES · CSP

This Article in Press is shared early to give you faster access to new research. It is citable and carries a permanent DOI. The final edited version will replace it automatically.



https://doi.org/10.1038/s41598-026-69109-x

Published online: 01 September 2026

scientific reports

Introduction

Escalating concerns regarding fossil-fuel dependence and associated environmental impacts have intensified the development of renewable energy technologies[1,2]. Among these technologies, concentrating solar power (CSP) is particularly attractive because solar irradiation is converted into thermal energy that can be supplied to high-temperature power-generation cycles[1,3]. When integrated with thermal energy storage (TES), CSP can provide dispatchable electricity beyond daylight hours and reduce the variability associated with solar resources[4,5]. For this reason, molten salts have become key working media in CSP plants, serving simultaneously as heat-transfer fluids and thermal-storage materials because of their favorable heat-storage capability and thermal stability at elevated temperatures[3,5]. Their low vapor pressure, stable behavior in the liquid state, and suitable flow performance under elevated-temperature conditions further support their use in solar-thermal systems[3,5,6]. Nevertheless, the performance and economic competitiveness of CSP systems remain strongly dependent on the thermophysical properties, freezing behavior, thermal stability, and operational reliability of the selected molten salt[3–6]. Alkali nitrate-nitrite salts are among the most established media for integrated heat transfer and energy storage. Compared with conventional organic heat-transfer oils, these inorganic salts permit operation at higher temperatures and can improve the thermodynamic efficiency of CSP cycles[7–9]. Solar Salt, composed of 60 wt% $NaNO_3$ and 40 wt% KNO_3, is widely used in commercial CSP facilities, but its melting/freezing temperature of approximately 220 °C creates a substantial risk of solidification during reduced-temperature or solar-off periods. This risk may cause flow obstruction, increase auxiliary heating demand, and raise parasitic energy consumption[4,6,10,11]. The ternary Hitec composition, containing 7 wt% $NaNO_3$, 53 wt% KNO_3, and 40 wt% $NaNO_2$, has attracted interest because its melting temperature is approximately 142 °C, which is nearly 80 °C lower than that of Solar Salt and therefore markedly reduces freeze-related operational concerns while offering greater flexibility under moderate-temperature operating conditions[3,6,12]. Hitec also exhibits relatively high specific heat capacity and low viscosity within the common CSP operating range, facilitating pumping and heat exchange[4,10,13]. Despite these advantages, its moderate heat capacity, limited thermal conductivity, and finite high-temperature stability constrain storage density, heat-transfer rates, and the usable operating window[1,6,8]. Since the amount of sensible heat stored is directly related to specific heat capacity and the operating-temperature span, even moderate improvements in these parameters can reduce the salt inventory required for a given storage duty. Likewise, enhanced thermal conductivity can shorten charging and discharging times and limit temperature gradients within storage components. Improving these properties without disrupting the phase and chemical integrity of the salt is therefore an important materials challenge for advanced CSP systems[10,13].

Nanoadditive incorporation has emerged as a promising strategy for overcoming the thermophysical limitations of molten salts. Specific heat capacity directly determines the sensible heat stored over a given temperature interval, whereas melting and solidification enthalpies describe the energy exchanged during phase transition. Thermal conductivity, in turn, governs the rate of heat exchange during charging and discharging[5,14]. Nanoparticles can influence these properties through their high specific surface area, the formation of salt-particle interfacial regions, heterogeneous nucleation effects, and changes in particle distribution and heat-transport pathways[1,4,6,10]. However, the resulting response depends strongly on additive chemistry, particle size, morphology, concentration, and dispersion stability. At suitable loadings, extended interfacial regions and conductive pathways may improve thermal-storage capacity, phase-change energetics, and heat-transfer performance. Above an optimum concentration, particle-particle interactions and agglomeration can reduce the effective interfacial area, disturb microstructural continuity, and suppress further enhancement[1,3–6,10,13]. Previous Hitec studies have consequently focused mainly on oxide nanoparticles such as Al_2O_3, TiO_2, CuO, and SiO_2, while conductive supports and layered additives have also been considered[1,3–5,10,13]. For example, oxide additions have produced improvements in specific heat capacity and phase-change behavior at relatively low concentrations, and coupling nanoparticles with metal foams has been used to strengthen heat recovery[4]. Hexagonal boron nitride has further demonstrated that boron-containing additives can modify specific heat capacity, phase-change enthalpy, and the accessible

operating-temperature interval of Hitec[8]. These studies establish the potential of nanoenhancement, but they also show that additive selection and concentration must be carefully optimized and that no single property should be evaluated independently of phase stability and thermal durability. For high-temperature molten-salt applications, an effective nanoadditive must retain structural and chemical stability during prolonged thermal exposure[1,10,15,16]. Boride ceramics are promising in this respect because of their refractory character, thermal resilience, and resistance to oxidation[8,15,17,18]. Hafnium diboride (HfB_2) combines a very high melting temperature with chemical inertness and high-temperature durability, making it a potential thermally conductive reinforcement for molten salts. Silicon hexaboride (SiB_6) also offers high-temperature stability and oxidation resistance, although its intrinsic thermal characteristics and particle behavior differ from those of transition-metal diborides[19–22]. These differences are important because the thermophysical response of a nanocomposite salt is governed not only by the intrinsic properties of the additive but also by its dispersion, interfacial contact, and tendency to form particle-rich networks or agglomerates within the salt matrix. The contrasting intrinsic characteristics and particle sizes of HfB_2 and SiB_6 therefore provide a useful basis for examining how additive chemistry and dispersion behavior influence the same Hitec system under identical preparation and testing conditions. Despite extensive research on nanoenhanced Hitec salts, the available literature remains dominated by oxide-based additives, and boride ceramics have received comparatively limited attention. Existing studies also frequently evaluate individual properties separately, which makes it difficult to establish whether improvements in thermal transport or energy storage are achieved while preserving phase stability, chemical integrity, and high-temperature durability. Based on the available literature, HfB_2 and SiB_6 have not previously been incorporated into Hitec and compared systematically within a unified experimental framework. The novelty of the present study lies in the direct evaluation of these two boride nanoparticle systems across the same concentration range and through a combined assessment of crystallographic structure, chemical bonding, morphology, elemental distribution, phase-change behavior, specific heat capacity, thermal conductivity, and degradation resistance. This integrated approach enables the observed thermophysical changes to be interpreted in relation to additive chemistry, particle distribution, and interfacial effects rather than from isolated measurements alone. It also allows the optimum additive level to be considered as a multi-property balance rather than as the concentration that maximizes only one thermal parameter. Accordingly, the present work investigates Hitec salts containing 0.5 to 2 wt% HfB_2 or SiB_6 nanoparticles prepared and characterized under identical conditions. X-ray diffraction and Fourier-transform infrared spectroscopy were used to determine whether nanoparticle incorporation altered the crystalline phases or chemical framework of Hitec. Field-emission scanning electron microscopy and energy-dispersive X-ray analysis were employed to examine morphology, additive distribution, and elemental homogeneity. Differential scanning calorimetry was used to quantify melting and solidification behavior and phase-dependent specific heat capacity, thermogravimetric analysis was applied to determine high-temperature stability, and the transient plane source method was used to measure thermal conductivity. The principal objective was to determine whether HfB_2 and SiB_6 can improve the energy-storage, heat-transfer, and thermal-stability characteristics of Hitec without inducing phase transformation or chemical degradation. A further objective was to identify how differences between the two borides produce distinct concentration-dependent responses and to establish their relative suitability for advanced CSP heat transfer and thermal energy storage applications.

Experimental procedure

Production of pure and nanoadditive molten salts

The preparation route for the pristine and nanoadditive-modified Hitec salts is summarized in Fig. 1. Sodium nitrate ($NaNO_3$), potassium nitrate (KNO_3), and sodium nitrite ($NaNO_2$), each with a purity of at least 99%, were supplied by Isolab GmbH, Germany. Before use, the precursor salts were dried at 120 °C for 24 h in a Weightlab laboratory oven (Istanbul, Türkiye) to remove residual moisture. They were then weighed according to the Hitec

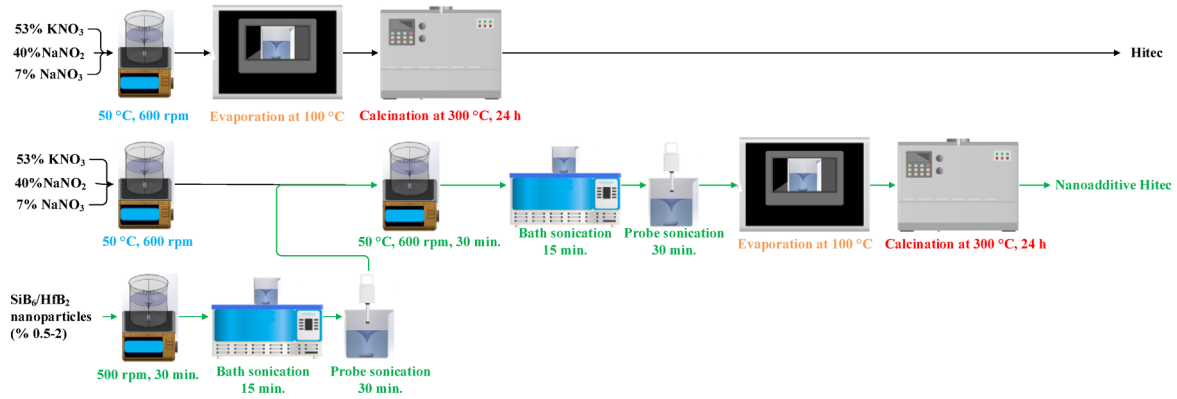


Fig. 1 Methodology of the research.

composition of 7 wt% $NaNO_3$, 53 wt% KNO_3, and 40 wt% $NaNO_2$. Beginning with the component present at the highest mass fraction, the constituents were sequentially dissolved in 100 mL of deionized water in a 500 mL glass beaker at 50 °C under magnetic stirring at 600 rpm. Each constituent was added only after complete dissolution of the preceding salt. The beaker was placed in a mineral-oil bath to maintain a stable temperature, which was monitored continuously using a probe. After a clear and homogeneous solution was obtained, water was removed at 100 °C. The recovered salt was heat treated at 300 °C for 24 h under argon in an Elektromag muffle furnace (Istanbul, Türkiye), cooled under controlled conditions to room temperature, and ground in an agate mortar to obtain a homogeneous powder. HfB_2 nanoparticles with 99.5% purity and an average particle size of approximately 50 nm and SiB_6 nanoparticles with 99% purity and an average particle size of approximately 40 nm were supplied by Nanografi Nano Technology, Ankara, Türkiye. Nanocomposites containing 0.5, 1.0, 1.5, and 2.0 wt% of either additive were prepared using the same salt formulation. The required amount of HfB_2 or SiB_6 was dispersed in 50 mL of deionized water by stirring at 500 rpm for 30 min, bath ultrasonication for 15 min, and probe ultrasonication for 30 min at 300 W and 40 kHz using a Bandelin Sonopuls system (Berlin, Germany). The suspension was gradually introduced into the Hitec solution under continuous stirring. The mixture was then maintained at 50 °C and 600 rpm for 30 min, treated again in an ultrasonic bath for 15 min, and probe-ultrasonicated for 30 min. Drying, heat treatment, cooling, and grinding were performed under the same conditions used for pristine Hitec. No visible sedimentation or phase separation was observed during preparation. Three independent batches were produced for each composition. The samples were designated Hitec, Hitec-x% HfB_2, and Hitec-x% SiB_6, where x represents the additive content by weight.

Structural and morphological characterizations

To minimize batch-related variation, approximately 5 g from each of the three independently prepared batches of a given composition were pooled and re-homogenized in an agate mortar. The resulting representative powders were used for structural, spectroscopic, and microstructural characterization. Previously reported structural and spectroscopic data for HfB_2[17], together with available reference data for SiB_6, were considered when interpreting additive-related features. X-ray diffraction measurements were performed using a Malvern Panalytical Empyrean diffractometer (Almelo, Netherlands) with Cu Kα radiation at 40 kV and 40 mA. Patterns were collected over a 2θ range of 10° to 80° at a scanning rate of 0.2° s^{-1}. The pristine and nanoadditive-containing Hitec salts, together with the individual HfB_2 and SiB_6 nanopowders, were examined under the same measurement conditions. The nanopowder patterns were also plotted separately using independent intensity scales because the normalization and vertical offset applied to the composite patterns reduced the visibility of weak additive-related diffraction features, particularly those of SiB_6. Fourier-transform infrared spectra were recorded from 400 to 4000 cm^{-1} using a Thermo Scientific Nicolet iS5 spectrometer (Waltham, MA, USA) to examine whether nanoadditive

incorporation altered the nitrate-nitrite bonding framework. Surface morphology, particle distribution, and elemental composition were evaluated by field-emission scanning electron microscopy coupled with energy-dispersive X-ray spectroscopy using a ZEISS Gemini 500 system (Oberkochen, Germany). EDX data were interpreted qualitatively and semi-quantitatively to verify the presence and spatial distribution of the additive-derived elements within the Hitec matrix.

Thermophysical measurements

All thermophysical instruments were checked and calibrated using certified standards in accordance with the manufacturers' procedures. Phase-change behavior and specific heat capacity were measured using a Hitachi DSC 7010 differential scanning calorimeter (Tokyo, Japan). Three independently synthesized samples were tested for each composition. Approximately 10 mg of material, weighed using a balance with a resolution of 0.00001 g, was sealed in a 40 µL aluminum crucible. Melting and solidification measurements were conducted from 0 to 300 °C under nitrogen at a heating and cooling rate of 10 °C min^{-1}. Nitrogen was used to minimize oxidation and moisture-related interference during thermal cycling. Two consecutive thermal cycles were applied, and data from the second cycle were used to represent the stabilized response. Specific heat capacity measurements were conducted from 0 to 400 °C in accordance with ASTM E1269. A sapphire standard was used for calibration, an empty crucible was used for baseline correction, and the reported C_p values represent the mean of three measurements for each composition. Data reduction was performed using the analysis software supplied with the instrument. Thermal stability was evaluated using a Shimadzu DTG-60AH thermogravimetric analyzer (Kyoto, Japan). Approximately 7 ± 1 mg of representative homogenized powder was placed in a 40 µL platinum crucible and heated from 50 to 800 °C at 10 °C min^{-1} under a controlled atmosphere. Equal portions from the independent synthesis batches were combined before testing to reduce batch-related variation. Thermal conductivity was measured by the transient plane source method using a Hot Disk TPS 2500 S Thermal Constants Analyzer (Hot Disk AB, Gothenburg, Sweden). The powders were compacted into cylindrical pellets 20 mm in diameter and 10 mm in thickness under a uniaxial pressure of 10 MPa to maintain consistent geometry and limit the influence of residual porosity. Three pellets were prepared and measured separately for each composition, and the mean value was reported. For transparency, the pristine Hitec sample and baseline thermophysical dataset used for comparison were also reported in an earlier study by the research group[23,24].

Results and discussion

The discussion of the experimental findings is arranged to establish a clear connection between nanoadditive incorporation and the resulting structural and thermophysical response of Hitec molten salt. The analysis first focuses on phase stability and microstructural features of the modified salt matrix, and then extends to the corresponding variations in melting-solidification behavior, thermal conductivity, specific heat capacity, and high-temperature stability. This organization provides a coherent framework for interpreting how structural and interfacial changes contribute to the overall performance of the nanocomposite salts.

Structural and morphological features

The macroscopic images displayed in Fig. 2 provide an initial visual assessment of the pristine and nanoadditive-containing Hitec pellets. All samples show a generally homogeneous external appearance, and no visible evidence of phase separation, severe sedimentation, or bulk-scale inhomogeneity is detected. Such macroscopic uniformity indicates that both HfB_2 and SiB_6 remained stably incorporated within the salt matrix throughout preparation and resolidification. In addition, the pellet appearance changes progressively with increasing additive content. The pristine Hitec sample is white, whereas the boride-containing samples become increasingly darker

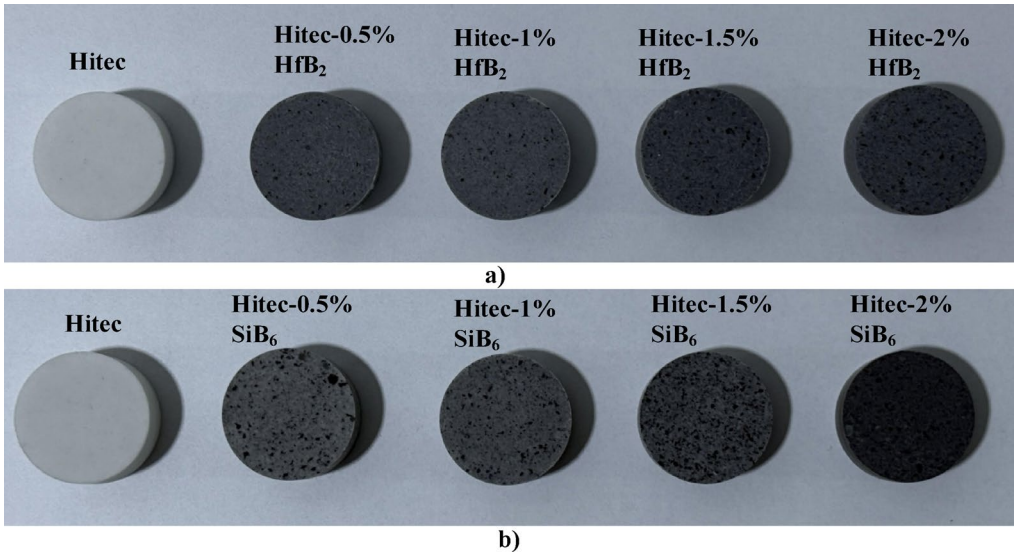


Fig. 2 Macro images of Hitec and nanoadditive Hitec salts.

as the loading level rises, reflecting the intrinsic dark color of HfB_2 and SiB_6. Because this color change occurs gradually and uniformly rather than through isolated dark patches, it also supports a relatively even distribution of the nanoparticles within the matrix. These visual observations therefore provide preliminary evidence that stable Hitec-based nanocomposite salts were successfully obtained.

The FT-IR spectra of the pristine and nanoadditive-modified Hitec salts are shown in Fig. 3. For a more reliable interpretation of the spectra obtained from the nanocomposite salts, the characteristic bands of the additive phases were considered first. In this respect, previously reported spectroscopic data for HfB_2 from our earlier boride-based molten-salt study were used as a reference framework, while literature data for SiB_6 were employed in the same comparative manner[17]. This procedure made it possible to distinguish additive-related spectral features from those originating from the Hitec salt matrix. For HfB_2, the band near 2364 cm^{-1} is assigned to C-H stretching vibrations, which may arise from carbon-containing surface species or residual surface contaminants associated with powder synthesis and processing[25,26]. A band observed in the low-wavenumber region at approximately 670 cm^{-1} is attributed to Hf–O stretching vibrations[26]. Its presence suggests limited surface oxidation of the HfB_2 particles and provides a recognizable FT-IR feature of the additive. Agreement between these features and earlier reports further supports the reproducibility of the HfB_2 nanopowder characteristics used in the present work[26,27]. In the SiB_6 spectrum, the band centered at about 2362 cm^{-1} is likewise associated with C-H stretching vibrations, whereas the bands located near 667, 995, and 1458 cm^{-1} are related to Si-O-Si and B-O vibrational modes[28]. These signals represent characteristic bonding features of the SiB_6 additive phase and therefore provide a useful basis for interpreting its contribution in the modified salt systems. The FT-IR spectrum of pristine Hitec is dominated by the band at approximately 824 cm^{-1}, which is characteristic of N-O vibrations in nitrate/nitrite salt systems. Additional absorptions around 1230, 1368, and 1764 cm^{-1} can be attributed to nitrate-group stretching and asymmetric vibrational modes associated mainly with the KNO_3 and $NaNO_3$ constituents of the eutectic composition[8,13]. The preservation of these characteristic bands confirms that the chemical identity of the Hitec matrix is consistent with the expected nitrate-nitrite system[5,8,13]. After addition of HfB_2 and SiB_6, the FT-IR spectra of the modified salts still retain the main nitrate/nitrite bands of pristine Hitec. No new absorption features attributable to newly formed compounds or bond structures are observed, indicating that nanoparticle addition does not induce a chemical reaction with the salt matrix and instead results in physical incorporation of the additives[5,8,29,30]. At the same time, weak bands within the 2360–2365 cm^{-1} region appear in the nanocomposite samples. Because these features coincide with the C-H-related bands identified for the nanopowders, they

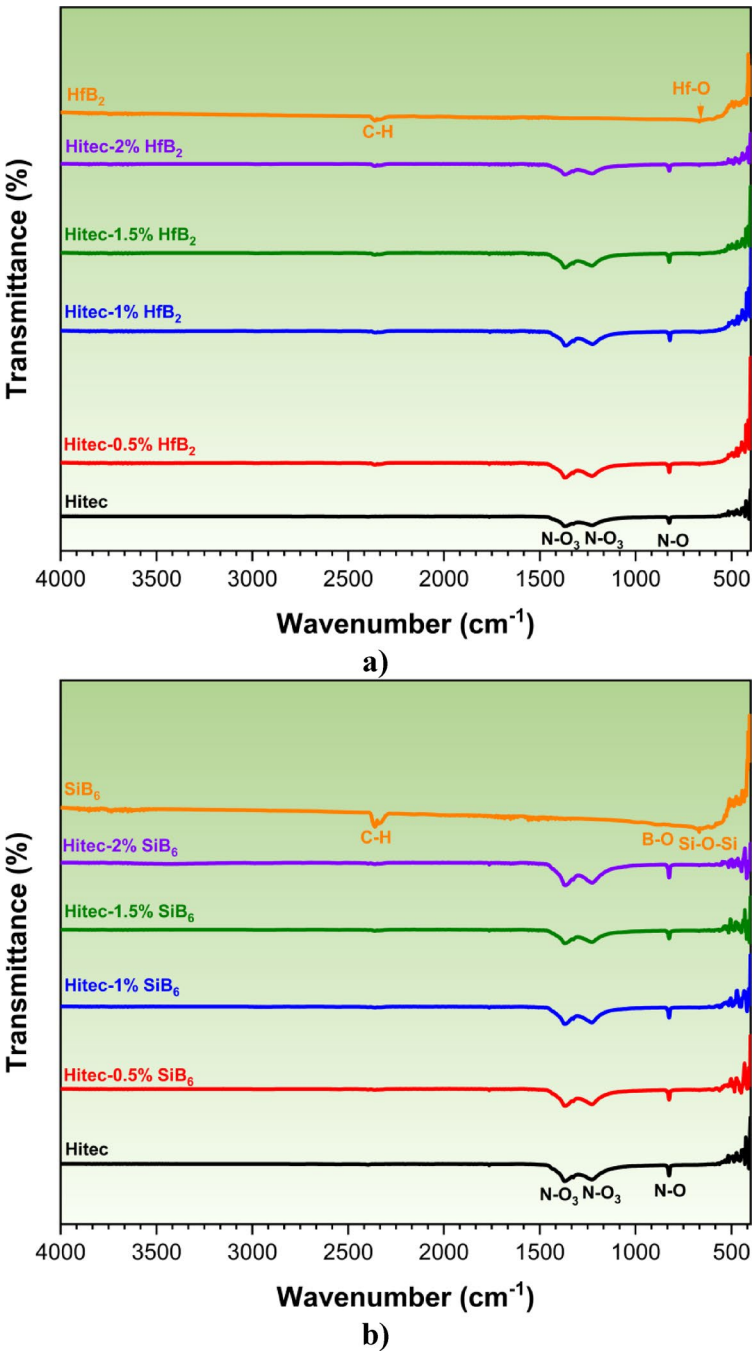


Fig. 3 FT-IR spectra of (**a**) HfB_2 nanopowder, pristine Hitec salt, and Hitec salts containing HfB_2, and (**b**) SiB_6 nanopowder, pristine Hitec salt, and Hitec salts containing SiB_6.

suggest that surface characteristics of the additives are reflected in the spectra of the modified salts. The gradual increase in the intensity of these weak bands with increasing additive amount may therefore be taken as qualitative evidence for successful nanoparticle incorporation. Not all bands characteristic of the isolated HfB_2 and SiB_6 powders can be distinctly resolved in the spectra of the nanocomposite salts. This can be explained by the low nanoparticle concentrations employed, the partial encapsulation of the particles within the surrounding salt phase, and the dominance of the strong nitrate-related absorptions of Hitec, which can obscure weaker additive-derived contributions[29–31]. Even so, slight changes in the intensity of some nitrate bands and small shifts in their peak positions with increasing additive loading point to the existence of interfacial, yet non-reactive, interactions between the salt and the nanoparticles. Such local interactions may alter the ionic environment around the

particles and produce modest changes in vibrational energy without leading to the formation of new chemical bonds[8,17,30]. Taken together, the FT-IR results show that the fundamental vibrational structure of Hitec is preserved after incorporation of HfB_2 and SiB_6. The persistence of the characteristic nitrate and nitrite bands across all modified samples demonstrates that the chemical framework of the salt remains essentially unchanged. In addition, the absence of extra bands related to newly generated species supports the view that the additives are physically embedded rather than chemically transformed within the matrix. Therefore, the FT-IR findings indicate that the thermophysical improvements observed in the nanocomposite salts are associated primarily with interfacial and microstructural effects, rather than with chemical alteration of the Hitec system.

The XRD patterns of pristine and nanoadditive-containing Hitec salts are presented in Fig. 4. For direct comparison among the investigated compositions, the patterns in Fig. 4a and b were normalized and vertically offset. However, this normalization compresses the differences in absolute diffraction intensity and makes weak or broad additive-related features difficult to distinguish, particularly for SiB_6. Therefore, the HfB_2 and SiB_6 nanopowder patterns are also presented separately in Fig. 4c and d using independent intensity scales. For pristine Hitec, the

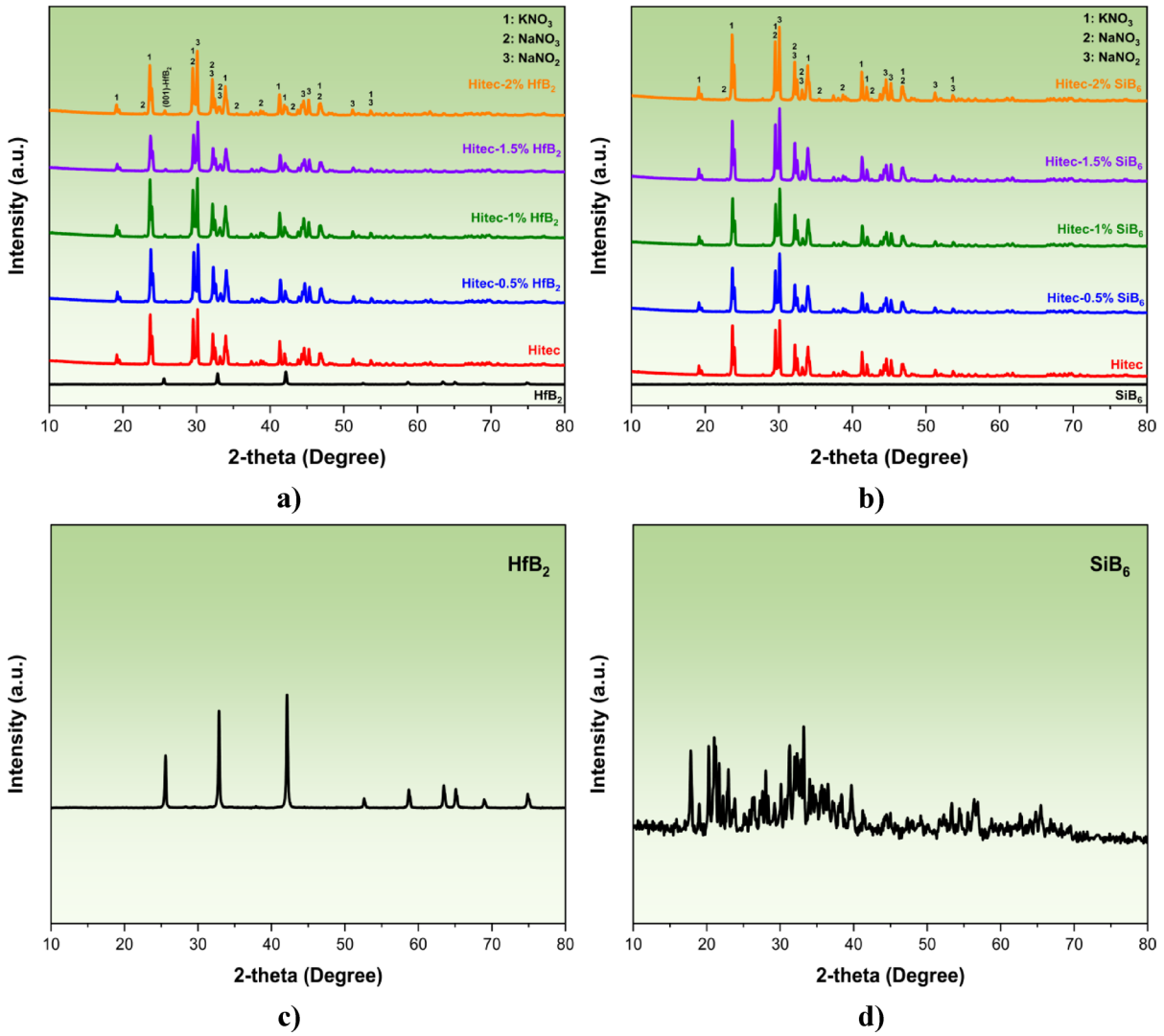


Fig. 4 XRD patterns of (**a**) HfB_2 nanopowder, pristine Hitec, and Hitec salts containing HfB_2, (**b**) SiB_6 nanopowder, pristine Hitec, and Hitec salts containing SiB_6, (**c**) the separately presented HfB_2 nanopowder, and (**d**) the separately presented SiB_6 nanopowder. The patterns in panels a and b are normalized and vertically offset for comparison, whereas the nanopowder patterns in panels c and d are presented using independent intensity scales to improve the visibility of their diffraction features.

principal diffraction features correspond to the characteristic reflections of KNO_3, $NaNO_3$, and $NaNO_2$, confirming the expected crystalline structure of the nitrate-nitrite eutectic salt. No additional peaks attributable to impurity phases or unintended crystalline products are observed, indicating that the synthesis route preserved the intended ternary salt composition. The diffraction profile obtained for pristine Hitec is also consistent with previously published data for comparable Hitec systems[32–36]. In the HfB_2-containing series, the major reflections of the Hitec matrix remain visible throughout the investigated concentration range, demonstrating that nanoparticle incorporation does not disrupt the principal crystalline framework of the salt. A weak diffraction feature is detected near $2\theta \approx 26°$, and its visibility increases gradually with increasing HfB_2 content[37,38]. This reflection is assigned to the (001) plane of HfB_2. Its comparatively low intensity is attributed to the limited additive concentration and the fine dispersion of the nanoparticles within the dominant crystalline Hitec matrix[39,40]. The separately presented HfB_2 nanopowder pattern in Fig. 4c provides a clearer representation of the diffraction features of the additive. The progressive visibility of the additive-related feature in the nanocomposite patterns supports the incorporation of HfB_2 while confirming that the structural identity of the host salt is maintained. A similar preservation of the principal Hitec reflections is observed in the SiB_6-containing compositions. Nevertheless, characteristic SiB_6-related reflections cannot be distinctly resolved in the normalized nanocomposite patterns. This result should not be interpreted as evidence that the additive was absent from the modified salt. The inability to distinguish individual SiB_6 peaks is more reasonably attributed to the low additive concentration range of 0.5 to 2 wt%, the relatively weak and broad diffraction response of the SiB_6 nanopowder, and the overlap of these features with the substantially stronger reflections of the Hitec matrix[29,39,40]. The separately presented SiB_6 nanopowder pattern in Fig. 4d allows its diffraction response to be examined more clearly than in the normalized and vertically offset composite presentation. When all diffraction patterns are evaluated together, no additional reflections associated with newly generated crystalline phases or phase-conversion products are detected in either additive series. This finding indicates that HfB_2 and SiB_6 incorporation does not produce new crystalline compounds within the Hitec system[35,39–42]. The minor variations observed in the relative intensities of the Hitec peaks are more plausibly related to differences in crystallization conditions, crystallite-size distribution, particle-induced microstructural heterogeneity, or preferred orientation rather than to a change in the overall phase composition[15,35,41,42]. When the XRD observations are interpreted together with the FT-IR results, it becomes clear that HfB_2 and SiB_6 incorporation does not disturb either the principal crystalline structure or the chemical framework of Hitec. Since neither technique reveals the formation of new crystalline or chemical species, the nanocomposite salts can be considered successfully prepared while preserving the structural and chemical integrity of the parent system. The retention of Hitec-specific reflections throughout the modified series further supports the preservation of phase stability after nanoparticle incorporation. Consequently, HfB_2 and SiB_6 can be regarded as physically integrated additives that form structurally stable Hitec-based nanocomposites without inducing phase transformation.

The FE-SEM micrographs and EDX spectra of the nanopowders, pristine Hitec, and the corresponding nanocomposite salts are presented in Figs. 5 and 6, while the EDX-derived elemental compositions are summarized in Table 1. To evaluate both the overall particle distribution and the local microstructural features, Fig. 5 presents paired low-magnification (5,000×) and high-magnification (30,000×) micrographs for each nanopowder and salt composition. Pristine Hitec exhibits a compact and continuous resolidified matrix composed of well-developed polygonal grains. The low-magnification image shows no major segregated region or bulk-scale microstructural discontinuity, whereas the high-magnification image reveals relatively smooth grain interiors and clearly distinguishable grain boundaries. This morphology is consistent with the EDX results of pristine Hitec, in which only the expected matrix elements, namely Na, K, O, and N, are detected[3,5,13,43]. The isolated HfB_2 and SiB_6 nanopowders both exhibit secondary agglomeration at the FE-SEM observation scale, although their local morphologies are distinguishable. HfB_2 consists predominantly of irregular granular aggregates, whereas the SiB_6 powder contains comparatively larger angular and plate-like fragments. Following HfB_2 incorporation, the low-magnification images confirm that the overall continuity of the Hitec matrix is retained throughout the investigated concentration range. The corresponding high-magnification images reveal additive-associated particulate regions located mainly along grain boundaries and intergranular junctions. At 0.5 and 1.0 wt% HfB_2, these features

https://doi.org/10.1038/s41598-026-69109-x

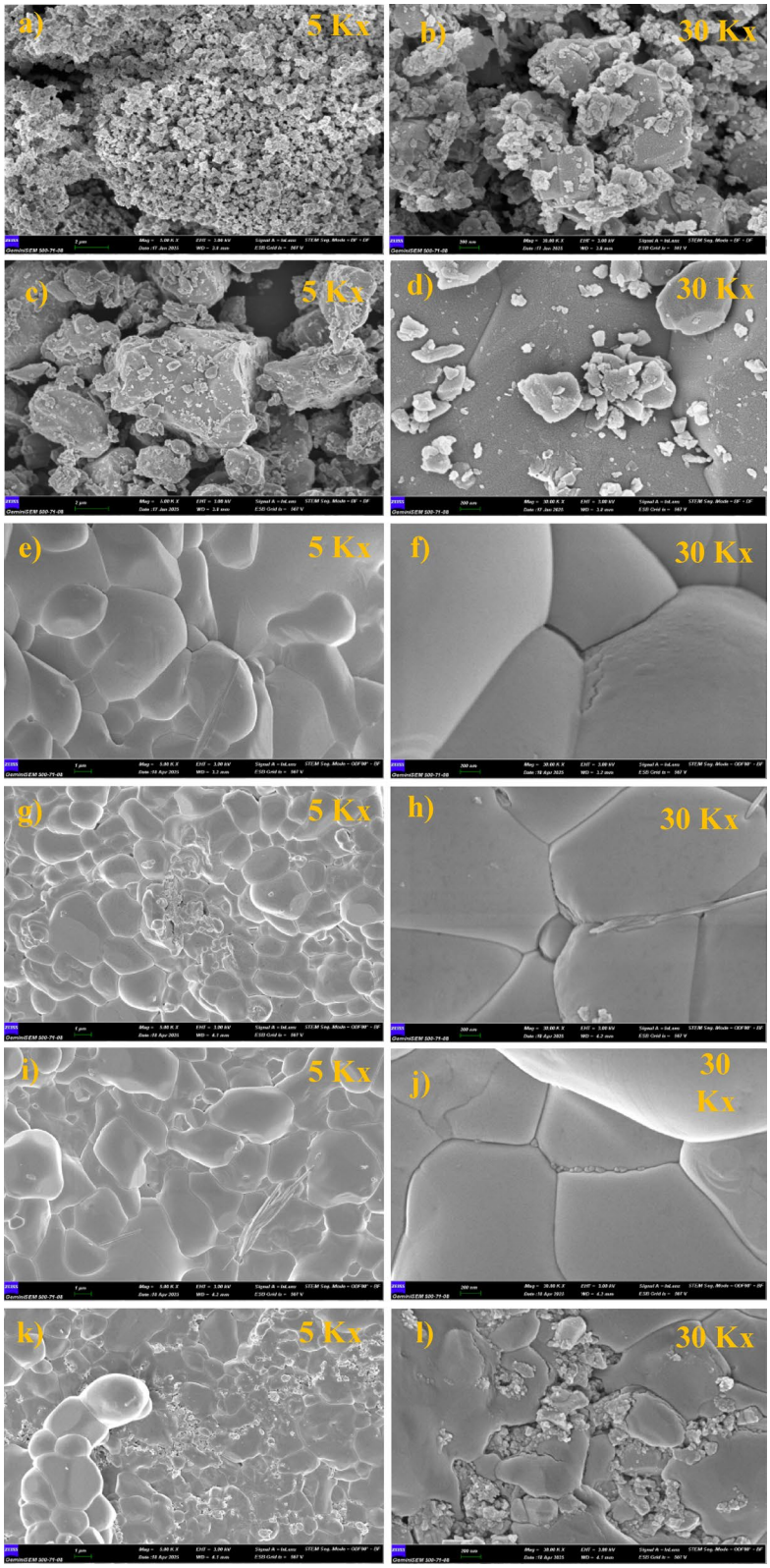


Fig. 5 Paired low- and high-magnification FE-SEM micrographs of (**a**, **b**) HfB_2 nanopowder, (**c**, **d**) SiB_6 nanopowder, (**e**, **f**) pristine Hitec, (**g**, **h**) Hitec-0.5 wt% HfB_2, (**i**, **j**) Hitec-1.0 wt% HfB_2, (**k**, **l**) Hitec-1.5 wt% HfB_2, (**m**, **n**) Hitec-2.0 wt% HfB_2, (**o**, **p**) Hitec-0.5 wt% SiB_6, (**q**, **r**) Hitec-1.0 wt% SiB_6, (**s**, **t**) Hitec-1.5 wt% SiB_6, and (**u**, **v**) Hitec-2.0 wt% SiB_6. The left and right panels of each pair correspond to 5,000× and 30,000× magnifications, respectively. Each micrograph includes its corresponding calibrated scale bar.

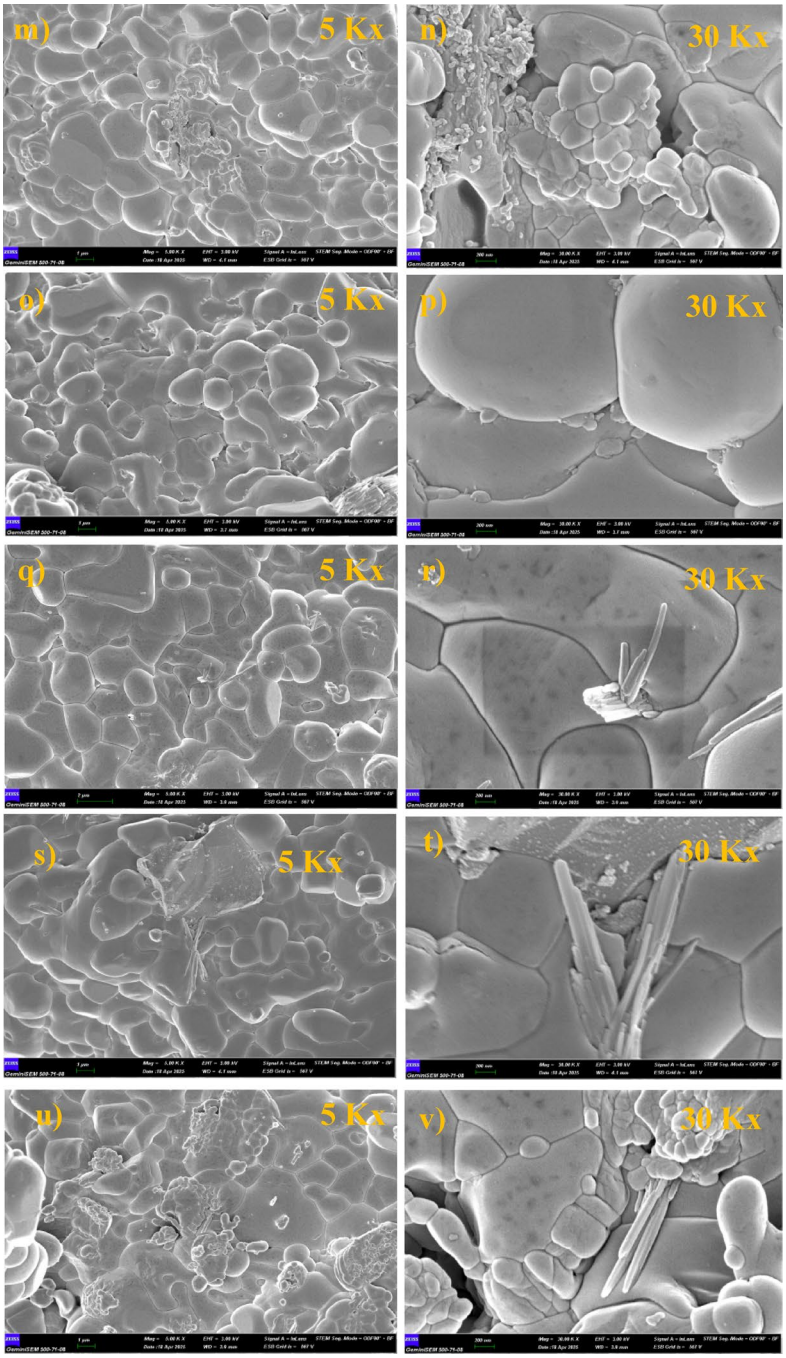


Fig. 5 (continued)

remain relatively discontinuous and locally confined, whereas particle-rich clusters become more evident at 1.5 and 2.0 wt%[13,43]. The progressive increases in B and Hf contents measured by EDX support the successful incorporation of HfB_2. The increasingly localized clusters observed at higher HfB_2 loadings are also consistent with stronger particle-particle interactions and a reduction in local dispersion uniformity[3,5,13,43]. The SiB_6-modified salts likewise retain a continuous Hitec matrix without evidence of bulk-scale phase separation. At 0.5 and 1.0 wt% SiB_6, the additive-associated features are observed mainly as locally embedded intergranular domains. At 1.5 and 2.0 wt%, coarser agglomerated regions and elongated or plate-like features become more evident[13,44,45]. The detection of B and Si throughout the SiB_6 series, together with the increasing Si content measured by EDX

https://doi.org/10.1038/s41598-026-69109-x

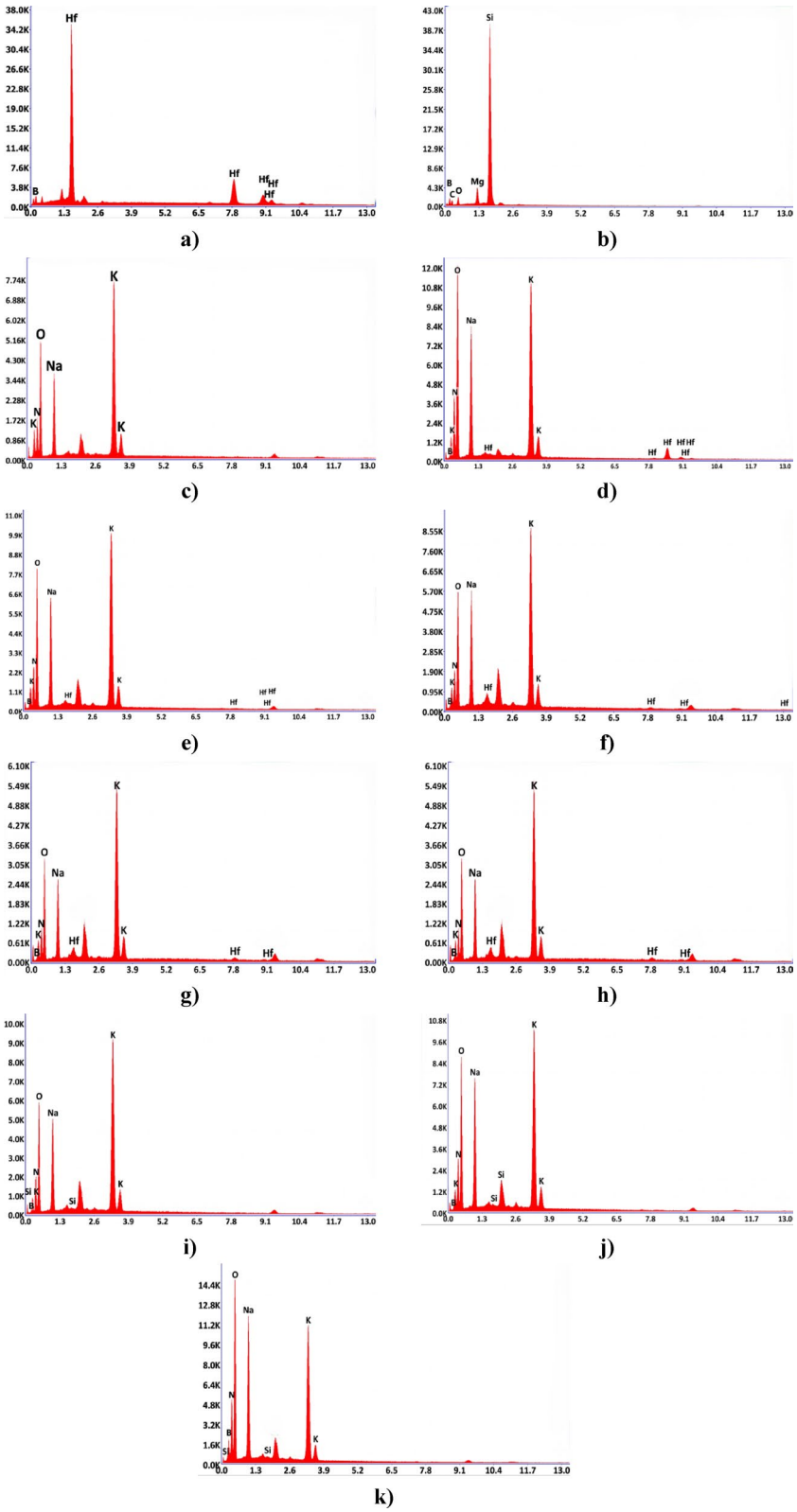


Fig. 6 EDX spectra of (**a**) HfB_2 nanoparticles, (**b**) SiB_6 nanoparticles, (**c**) Hitec, (**d**) Hitec-0.5% HfB_2, (**e**) Hitec-1% HfB_2, (**f**) Hitec-1.5% HfB_2, (**g**) Hitec-2% HfB_2, (**h**) Hitec-0.5% SiB_6, (**i**) Hitec-1% SiB_6, (**j**) Hitec-1.5% SiB_6 and (**k**) Hitec-2% SiB_6.

Table 1 EDX-derived elemental compositions (wt%) of the nanopowders, pristine Hitec salt, and Hitec nanocomposites.

Sample	B	Hf	Si	*N*	O	Na	K
Hitec	–	–	–	21.28	40.72	13.93	24.08
HfB_2	32.07	67.93	–	–	–	–	–
SiB_6	52.62	–	23.10	–	5.70	–	–
Hitec-0.5% HfB_2	5.32	0.31	–	20.45	41.92	15.29	16.71
Hitec-1% HfB_2	7.78	0.58	–	18.56	38.15	14.99	19.94
Hitec-1.5% HfB_2	9.49	1.37	–	18.29	34.71	15.36	20.77
Hitec-2% HfB_2	10.24	3.27	–	17.97	34.21	12.00	22.31
Hitec-0.5% SiB_6	0.01	–	0.11	19.72	39.40	15.92	24.85
Hitec-1% SiB_6	0.38	–	0.20	20.66	41.77	16.63	20.36
Hitec-1.5% SiB_6	0.09	–	0.24	20.36	40.46	18.31	20.54
Hitec-2% SiB_6	1.61	–	0.36	20.19	43.60	19.51	14.72

as the additive loading rises, further confirms the incorporation of the SiB_6 phase. The paired low- and high-magnification images also provide a more direct comparison between the two 2.0 wt% compositions. Both systems contain locally agglomerated regions; however, the HfB_2-containing sample predominantly exhibits localized granular particle-rich clusters, whereas the SiB_6-containing sample contains more morphologically heterogeneous regions incorporating both rounded and elongated features. The distinction between the two systems is therefore based on the directly observed morphology and spatial arrangement rather than on an assumption that either composition possesses completely homogeneous nanoparticle dispersion[44,45]. For all modified compositions, Na, K, O, and N remain the dominant matrix elements, and no unexpected foreign elements are detected. Together with the XRD and FT-IR findings, the FE-SEM and EDX results indicate that nanoadditive incorporation modifies the physical distribution and interfacial organization of the resolidified salt without providing evidence of chemical transformation. The paired low- and high-magnification examination therefore provides a more reliable microstructural basis for interpreting the concentration-dependent thermophysical behavior of the HfB_2- and SiB_6-containing Hitec salts[3,5,13,43–45].

The EDX elemental maps shown in Fig. 7 illustrate how the matrix elements and nanoadditive-related elements are spatially distributed in pristine and modified Hitec salts after melting and resolidification. In the pristine Hitec sample, the signals of N, O, Na, and K are spread uniformly over the examined region, with no obvious enrichment or depletion zones. This homogeneous distribution indicates that the nitrate-nitrite constituents remain well mixed within the matrix and that the solidified salt does not exhibit elemental segregation, in agreement with previous reports on Hitec-based systems[5,8,13]. A similar overall distribution of the host elements is retained in the sample containing 2 wt% HfB_2, showing that the incorporation of the additive does not disturb the intrinsic elemental arrangement of the Hitec matrix. In addition to the matrix-related signals, Hf is detected at several positions across the mapped area. These Hf-containing regions are dispersed within the salt phase rather than forming large continuous segregated domains, which supports effective incorporation of the HfB_2 nanoparticles. By contrast, the boron signal remains weak in the mapping images, which is expected because boron has a low atomic number and is difficult to detect reliably by EDX[17,40]. For this reason, the presence and spatial distribution of the HfB_2 phase are more convincingly reflected by the Hf map. The mapping results for the Hitec sample containing 2 wt% SiB_6 again show that the major matrix elements remain homogeneously distributed, confirming that the nitrate-nitrite framework of the salt is maintained after additive incorporation. The Si map, however, reveals fine and broadly distributed Si-containing regions throughout the matrix, indicating successful dispersion of the SiB_6 nanoparticles. Compared with the more localized Hf-rich regions observed in the HfB_2-modified salt, the Si signal is more diffuse, which is consistent with the smaller particle size of SiB_6 and its greater tendency to become surrounded by the molten salt during processing, leading to a more uniform encapsulated distribution. The weak visibility of boron in both additive systems should not be taken as evidence of incomplete nanoparticle incorporation; rather, it reflects the inherent difficulty of detecting light elements by EDX. When the mapping images are interpreted together with the quantitative EDX data in Table 1, the systematic increase of Hf and

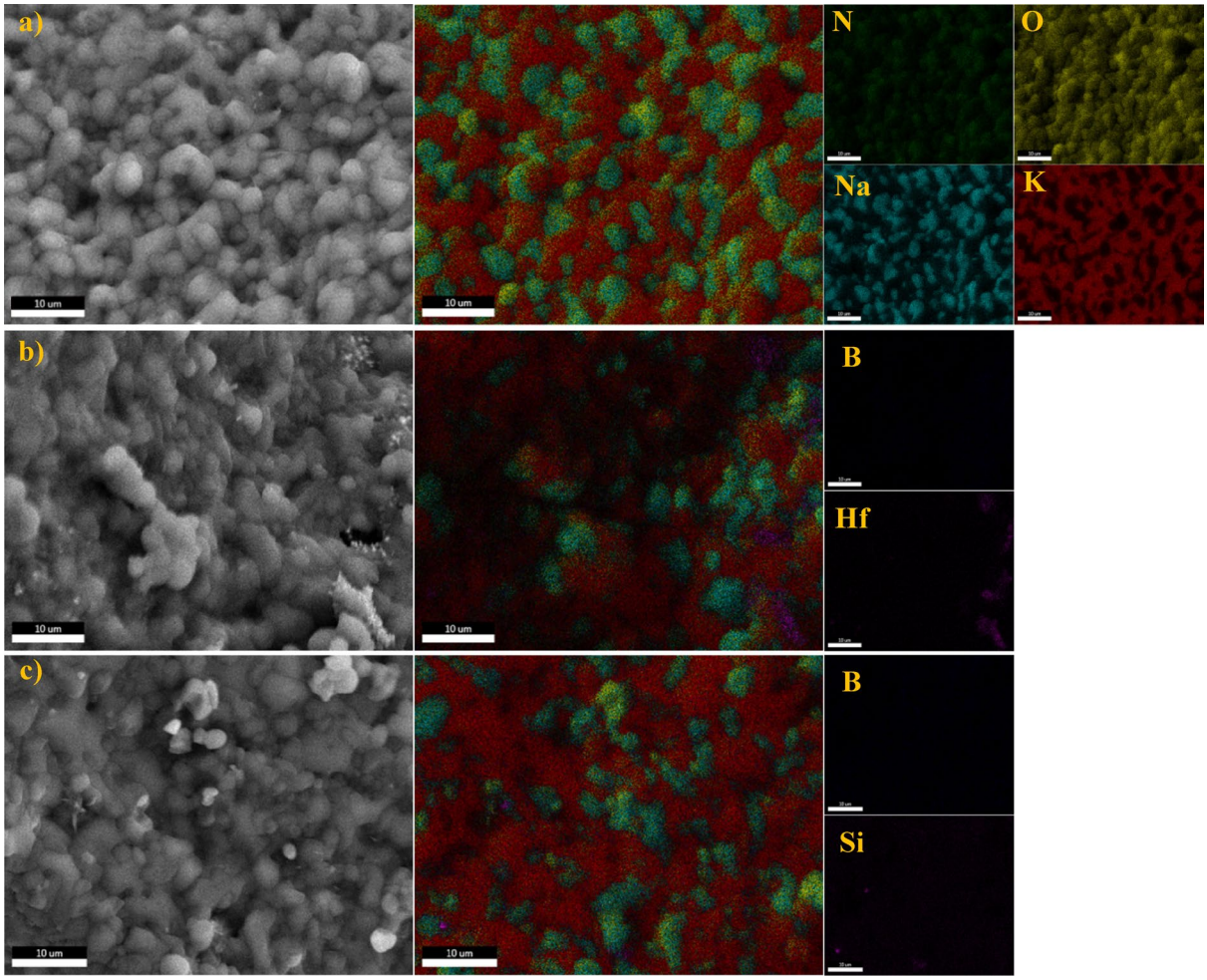


Fig. 7 SEM images and EDX elemental maps of (**a**) pristine Hitec, (**b**) Hitec–2.0 wt% HfB_2, and (**c**) Hitec–2.0 wt% SiB_6. Individual maps show N, O, Na, and K in (**a**), B and Hf in (**b**), and B and Si in (**c**); all panels within each group correspond to the same observation area and include 10 µm scale bars.

Si with additive loading provides further confirmation that the nanoparticle phases are successfully introduced into the Hitec matrix[3,5]. Combined with the FE-SEM observations, the mapping data indicate that HfB_2 tends to produce more localized additive-rich regions associated with interfacial networks and partial clustering, whereas SiB_6 shows a finer and more homogeneous spatial distribution. These differences are better explained by particle-size and surface-related effects than by any change in chemical composition or phase stability. No elemental signatures suggesting contamination or secondary phases are detected in any sample. Overall, the EDX mapping results confirm that both HfB_2 and SiB_6 are incorporated without disturbing the elemental uniformity of the host salt, and they provide a microstructural basis for interpreting the later differences in thermophysical behavior.

DSC behaviour

The DSC profiles presented in Fig. 8, together with the thermal values summarized in Table 2, describe the phase-transition behavior of the investigated salts. In the case of pristine Hitec, a weak thermal response is observed close to 100 °C before the main melting region. This faint feature is most likely associated either with a minor solid-solid rearrangement within the multicomponent nitrate-nitrite system or with low-temperature effects related to the removal of residual moisture[1,32,46]. The dominant thermal events correspond to the melting

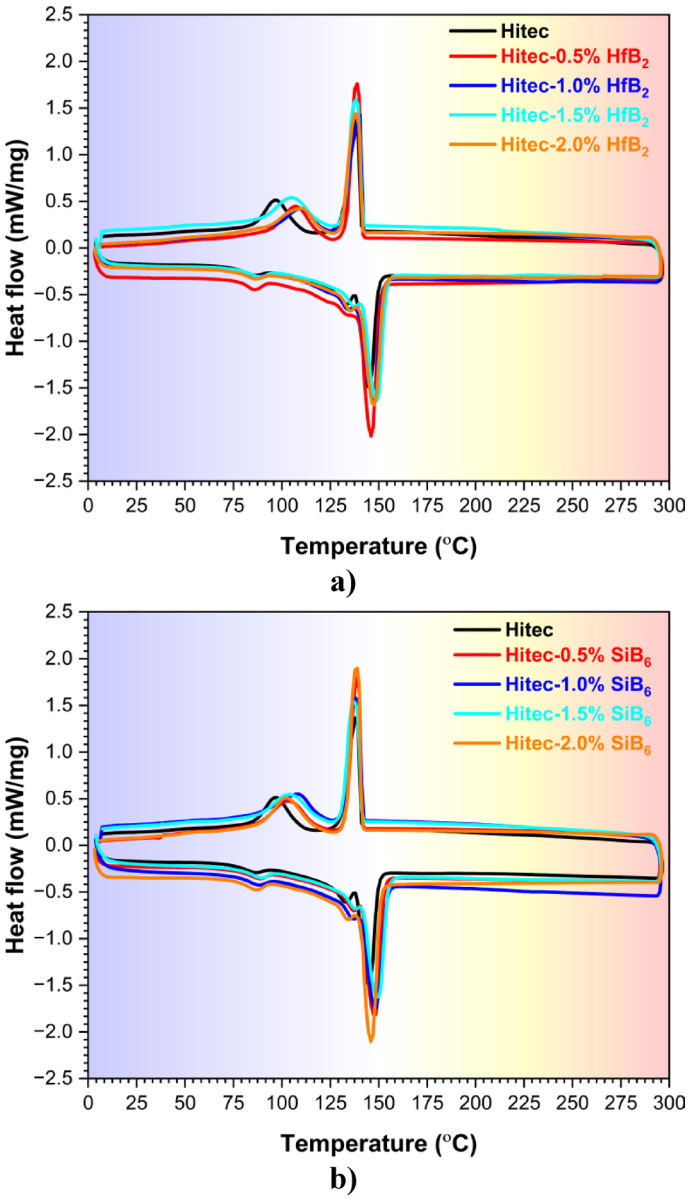


Fig. 8 Differential scanning calorimetry heating-cooling profiles of (**a**) pristine Hitec and HfB_2-containing compositions, and (**b**) pristine Hitec and SiB_6-containing compositions.

Table 2 Average phase-change parameters obtained from differential scanning calorimetry for pristine and nanoadditive-modified Hitec salts.

Additive ratio (wt%)-nanoadditive	T_{mon} (°C)	T_{mp} (°C)	ΔH_{entm} (J/g)	T_{son} (°C)	T_{sp} (°C)	ΔH_{ents} (J/g)	ω_{melt} %	ω_{sol} %	ΔT (°C)
0	138.6	144.6	76.2	143.9	140.3	71.6	100.0	100.0	4.3
0.5-HfB_2	139.5	147.0	89.4	144.5	136.7	88.0	117.3	122.9	10.3
1.0-HfB_2	139.2	148.2	89.8	144.2	136.1	90.7	117.8	126.7	12.1
1.5-HfB_2	140.3	147.6	90.1	144.1	137.1	91.6	118.2	127.9	10.5
2.0-HfB_2	140.5	148.2	90.6	146.9	137.2	92.2	118.9	128.8	11.0
0.5-SiB_6	141.2	147.4	92.6	146.4	139.1	97.3	121.5	135.9	8.3
1.0-SiB_6	140.9	148.1	95.6	146.1	137.3	96.8	125.5	135.2	10.8
1.5-SiB_6	140.5	147.1	93.5	145.3	137.7	94.2	122.7	131.6	9.4
2.0-SiB_6	141.2	146.4	92.8	145.8	138.6	93.4	121.8	130.4	7.8

and solidification transitions of the salt. During heating, pristine Hitec exhibits an onset melting temperature (T_{mon}) of 138.6 °C and a peak melting temperature (T_{mp}) of 144.6 °C, with a melting enthalpy (ΔH_{entm}) of 76.2 J/g. The baseline values for pristine Hitec were taken from our previously published dataset[23] to ensure that all comparisons reported in this study are based on the same reference dataset. During cooling, the onset solidification temperature (T_{son}), peak solidification temperature (T_{sp}), and solidification enthalpy (ΔH_{ents}) are 143.9 °C, 140.3 °C, and 71.6 J/g, respectively. These values confirm that the thermal transition behavior of pristine Hitec is stable and reproducible, and they remain compatible with previously published data for comparable Hitec-based systems[4,8,32,47]. The cooling profiles also contain a second exothermic signal besides the main solidification peak. This feature indicates that crystallization is not completed in a single stage, but instead develops through successive thermal events[4,17,32,47]. Such behavior is reasonable for a eutectic salt containing multiple components. One possible explanation is that a specific phase or sub-composition crystallizes first, after which further crystallization proceeds as the composition of the remaining liquid shifts toward the eutectic domain. Another possible contribution may come from structural rearrangements within the solid phase or from post-solidification solid-solid transformations[4,17,32,47]. For the nanocomposite Hitec salts, the effective contribution of the material to the phase-transition process was quantified by calculating the melting and solidification mass fractions using the equations given below[15,29]:

$$w_m = \frac{\Delta H_{entm,\,nano}}{\Delta H_{entm,\ Hitec}} * 100 \tag{1}$$

$$w_s = \frac{\Delta H_{ents,\,nano}}{\Delta H_{ents,\ Hitec}} * 100 \tag{2}$$

The symbols used in these equations distinguish the enthalpy values of the modified salts from those of the unmodified reference composition. In this context, $\Delta H_{entm,\,nano}$ and $\Delta H_{ents,\,nano}$ correspond to the melting and solidification enthalpies of the nanocomposite formulations, whereas ΔH_{entm},Hitec and ΔH_{ents},Hitec denote the same thermal quantities for pristine Hitec. The reference Hitec sample exhibited a melting enthalpy of 76.2 J/g. After addition of HfB_2, the melting enthalpy shifted upward and fell within the interval of 89.4–90.6 J/g. The solidification enthalpy followed the same overall direction, increasing to values between 88.0 and 92.2 J/g. The resulting enhancement is also evident from the ωm and ωs values presented in Table 2, which were found to lie in the approximate ranges of 117–119% and 123–129%, respectively. The fact that the changes in phase-change temperatures remain relatively limited while the enthalpy values exhibit a pronounced improvement suggests that the nanoadditive primarily enhances the latent heat storage capacity through interfacial effects, rather than altering the inherent phase-change temperature window of the system[17,48]. It is considered that the formation of heterogeneous nucleation sites by HfB_2 nanoparticles within the salt matrix facilitates more effective ionic rearrangement during melting and solidification, thereby enabling enhanced energy exchange[39,49,50]. Nevertheless, the fact that the enthalpy enhancement in the HfB_2-added nanocomposites does not increase linearly with additive loading suggests that the response is sensitive to the dispersion homogeneity of the nanoparticles[3,5,51]. At lower loadings, a more uniform dispersion and a larger effective interfacial area are expected, whereas increasing the additive content can promote agglomeration and thereby reduce the active surface area. This microstructural heterogeneity is considered to contribute to a more pronounced secondary exothermic signal in the cooling curves or to a broadened solidification behavior[3,5,15,51]. In the SiB_6-containing nanocomposites, the phase-change temperatures changed only marginally relative to pristine Hitec, whereas the enthalpy response exhibited a distinct concentration-dependent optimum. The melting enthalpy increased from 92.6 J/g at 0.5 wt% to a maximum of 95.6 J/g at 1.0 wt%, before decreasing to 93.5 and 92.8 J/g at 1.5 and 2.0 wt%, respectively. The solidification enthalpy reached its highest measured value at 0.5 wt% SiB_6 (97.3 J/g), remained nearly comparable at 1.0 wt% (96.8 J/g), and subsequently declined to 94.2 and 93.4 J/g at 1.5 and 2.0 wt%, respectively. Therefore, although the exact maximum differs slightly between the heating and cooling processes, both transitions identify 0.5–1.0 wt% as the most favorable SiB_6 concentration range. This behaviour contrasts with that of the HfB_2 series, in

which both enthalpies increase monotonically across the entire range studied, from 89.4 to 90.6 J/g and from 88.0 to 92.2 J/g, respectively, with no internal optimum or subsequent decline observed within the investigated concentration range. Since the two additives were introduced on the same mass basis and processed under identical conditions, this difference indicates that the concentration dependence is governed by the characteristics of the additive particles rather than by the additive mass alone. At these low-to-intermediate additive levels, the comparatively small SiB_6 particles can provide an extensive and accessible salt-particle interfacial area without severe particle crowding. During melting, these interfaces can modify the local ionic environment and facilitate the rearrangement of the nitrate-nitrite species, thereby supporting more effective energy absorption. During cooling, well-dispersed particles can additionally provide spatially distributed heterogeneous nucleation sites, promoting effective crystallization and thermal-energy release throughout the salt matrix[17,39,48,50]. The slight difference between the melting optimum at 1.0 wt% and the solidification maximum at 0.5 wt% is plausibly associated with the different kinetic sensitivities of melting and crystallization; nevertheless, both results indicate that the beneficial interfacial contribution is strongest before extensive particle-particle interaction develops. When the SiB_6 loading exceeds 1.0 wt%, the reduction in interparticle distance and the high surface energy of the fine particles increase the probability of particle-particle interaction and agglomeration. This interpretation is consistent with the morphological observations of Sect. 3.1, in which additive-associated agglomerated regions are present in the compositions containing the highest SiB_6 contents. Under these conditions, a greater fraction of the nanopowder becomes incorporated into particle-rich clusters rather than remaining available as individually accessible salt-particle interfaces. This clustering reduces the effective interfacial area per unit additive mass, produces locally heterogeneous particle-rich and particle-poor regions, and can restrict the continuity of ionic rearrangement and crystal growth during the phase transition[3,5,17,39]. Consequently, further SiB_6 addition does not provide a proportional increase in phase-change energy and instead causes the observed decreases in both melting and solidification enthalpies. The resulting non-linear trend therefore reflects a balance between beneficial interfacial and nucleation effects at 0.5–1.0 wt% and increasingly detrimental agglomeration effects at 1.5–2.0 wt%, rather than a direct dependence on additive quantity alone.

The degree of supercooling (ΔT) was calculated from the difference between the peak melting temperature and the peak solidification temperature, as expressed in Eq. 3[15]:

$$\Delta T = T_{mp} - T_{ms} \tag{3}$$

For pristine Hitec, the degree of supercooling was measured as ΔT = 4.3 °C. After HfB_2 addition, ΔT increased to 10.3–12.1 °C, whereas the SiB_6-containing compositions exhibited ΔT values in the range of 7.8–10.8 °C. The higher supercooling observed in both additive series relative to pristine Hitec indicates that solidification shifts toward lower temperatures. This behavior suggests a greater nucleation barrier and a stronger role of kinetic limitations during crystallization rather than equilibrium-driven solidification[17,48]. One possible explanation is that the interfacial layers created around the nanoparticles interfere locally with the ordering of ions into a stable crystal lattice, allowing the molten phase to persist for a longer time. From the viewpoint of microstructure, agglomerates and chain-like particle assemblies formed at higher additive contents may interrupt the continuity of crystal growth, so that some regions favor nucleation while others delay it[39,49,50,52,53]. When the HfB_2 and SiB_6-added nanocomposites are considered together, both systems are found to enhance the latent heat storage capacity while largely preserving the phase-change temperatures of pristine Hitec. However, the SiB_6 series exhibits a more pronounced enthalpy enhancement, as reflected by higher ω_m and particularly ω_s values. This point is particularly important from an application perspective, since the SiB_6-modified compositions combine a comparatively lower supercooling penalty with markedly stronger latent-heat enhancement, making their overall phase-change performance more attractive than that of the HfB_2 series. In contrast, the HfB_2-added samples display higher ΔT values, indicating a stronger supercooling tendency. This difference can be attributed to variations in particle size and specific surface area, which influence the intensity of interfacial interactions, as well as to differences in dispersion homogeneity and the relative dominance of agglomeration effects within the microstructure[17,54,55].

Although a rise in ΔT points to a stronger supercooling tendency, this effect should not be treated on its own as the main limitation of the present systems. The nanocomposite salts continue to operate within the characteristic phase-transition interval of pristine Hitec, while at the same time showing marked increases in both melting and solidification enthalpies. In practical terms, this indicates that a moderate supercooling penalty is accompanied by a substantial improvement in thermal energy storage capability and phase-change efficiency. As a result, the overall thermophysical performance remains advantageous, especially in compositions where the increase in ΔT is compensated by significant gains in ΔH_{ent} and ω values.

Figures 9 and 10 summarize the DSC trends discussed above. The limited spread of the error bars confirms good measurement repeatability. In both additive series, the characteristic phase-transition temperatures remain within a narrow interval close to those of pristine Hitec, whereas the melting and solidification enthalpies are enhanced. The HfB_2 series exhibits a gradual increase throughout the investigated concentration range, while the

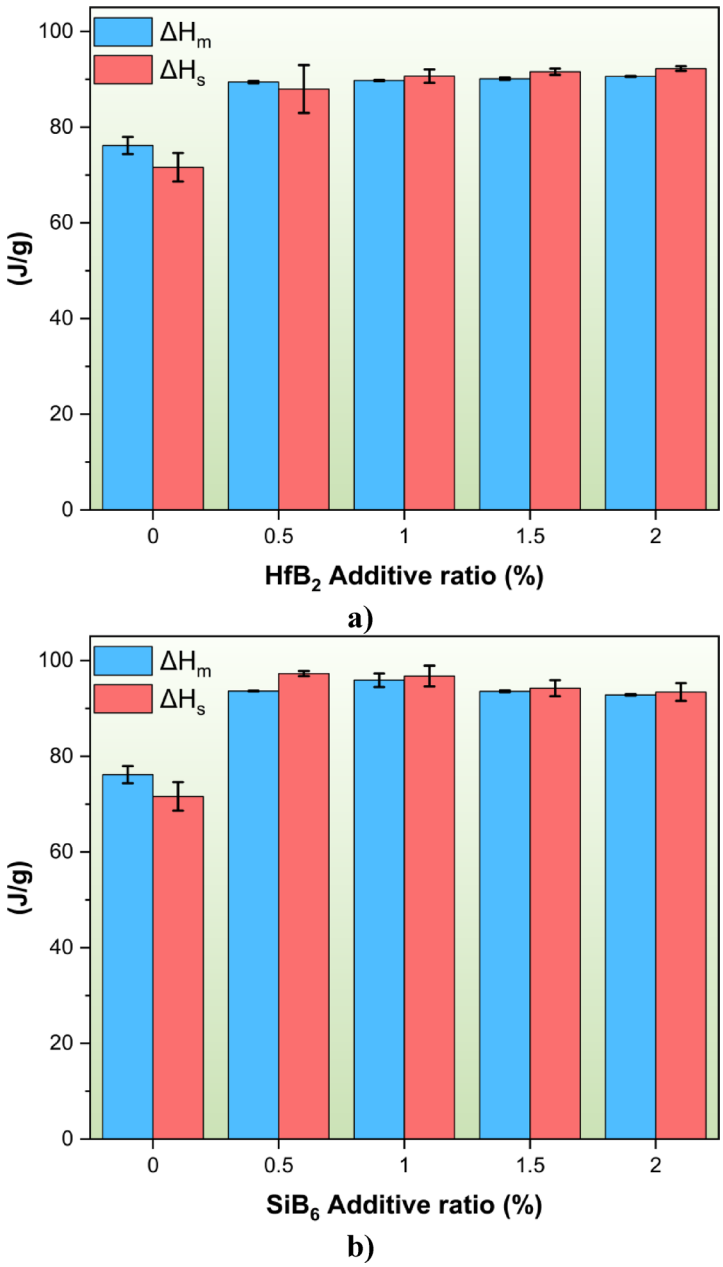


Fig. 9 Variation in melting and solidification enthalpy parameters with additive loading for (a) HfB_2-containing and (b) SiB_6-containing Hitec salts.

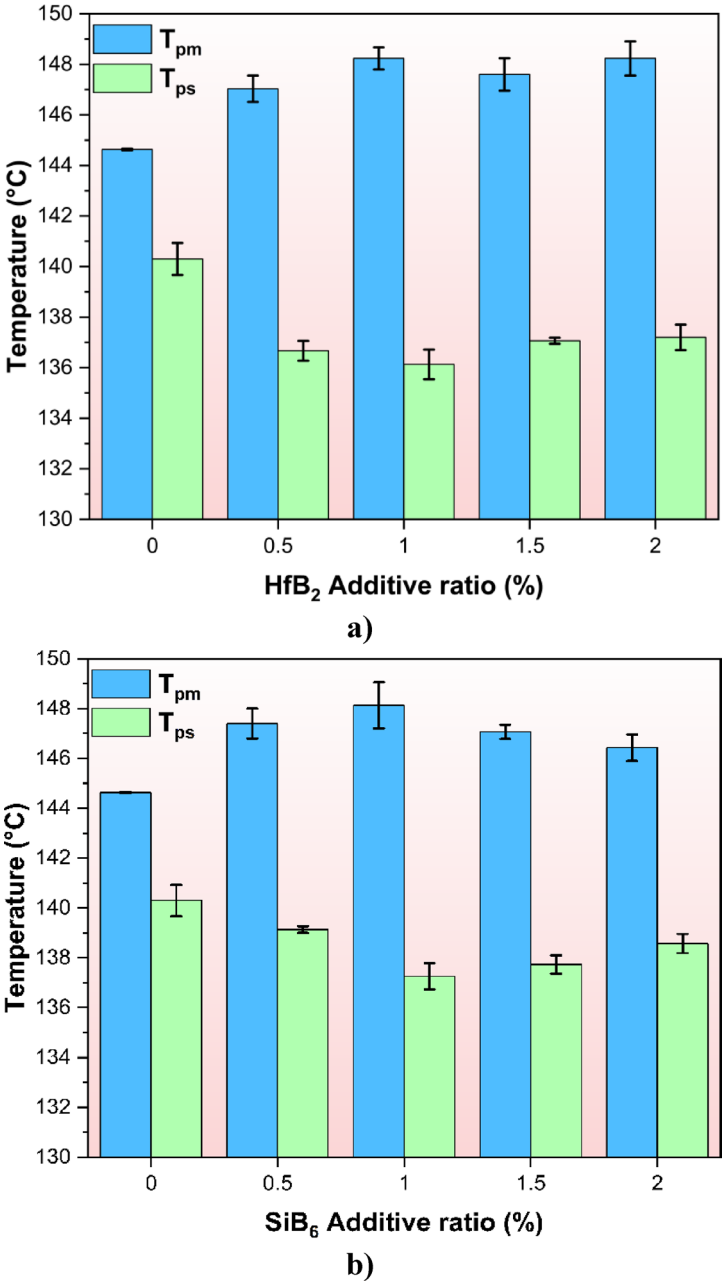


Fig. 10 Influence of additive concentration on phase-transition temperature parameters for (a) HfB_2-modified and (b) SiB_6-modified Hitec salts.

SiB_6 series shows its most favorable response at 0.5–1.0 wt% followed by a decline at higher loadings. These figures therefore confirm that the magnitude and concentration dependence of the enthalpy enhancement are additive-specific, while the fundamental phase-transition window of Hitec remains largely preserved[17,43].

Thermal conductivity behaviour

Figure 11 compares the room-temperature thermal conductivity behavior of pristine Hitec with that of the HfB_2 and SiB_6-modified compositions. The measured conductivity values are presented together with their corresponding error bars, while the calculated enhancement percentages are also given based on Eq. 4[17]. The limited spread of the error bars indicates good measurement consistency and suggests that the observed variations mainly arise from nanoadditive incorporation rather than experimental uncertainty.

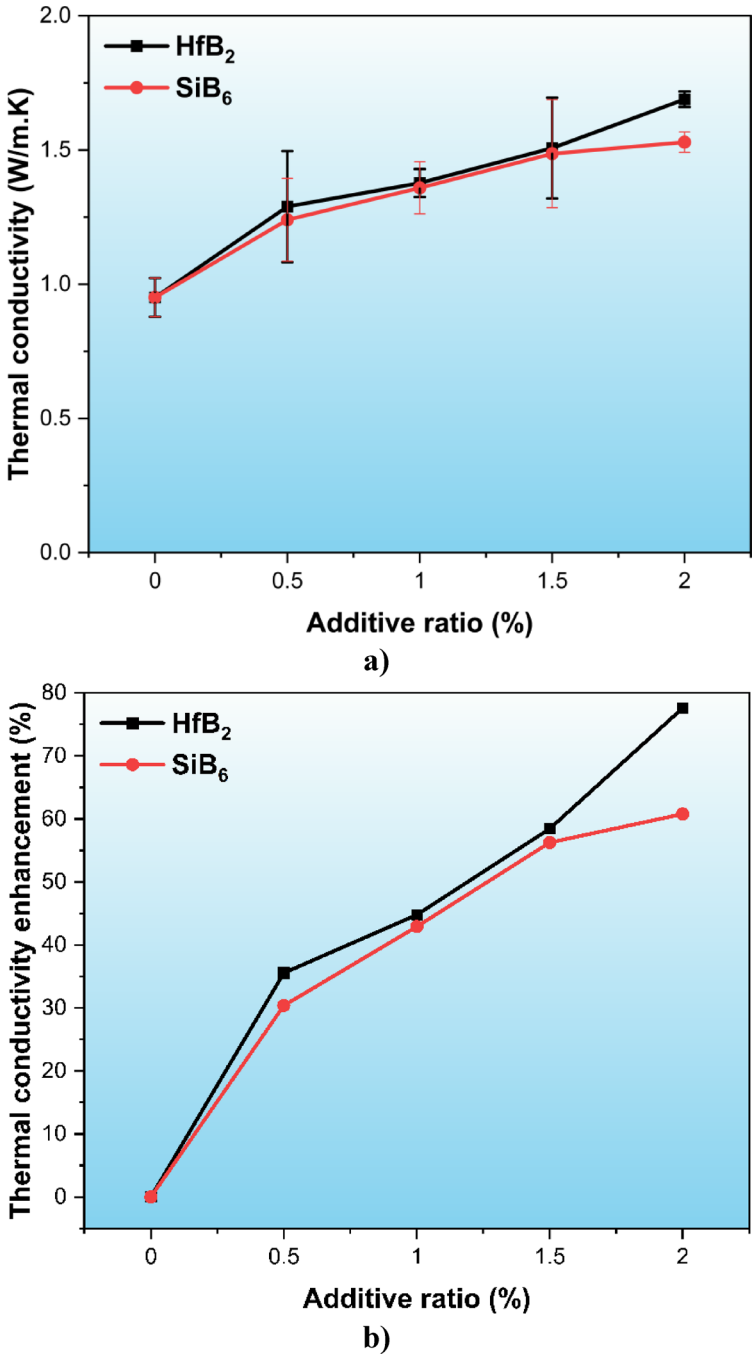


Fig. 11 (**a**) Measured thermal conductivity (**k**) of pristine Hitec and the modified salt compositions, and (**b**) calculated conductivity enhancement (%) for the same systems.

$$kenhancement\ \% = \left(\frac{k_{nano} - k_{Hitec}}{k_{Hitec}}\right) * 100 \quad (4)$$

In Eq. 4, k_{nano} denotes the thermal conductivity of the nanoadditive-containing composition, whereas k_{Hitec} denotes that of pristine Hitec. The thermal conductivity of pristine Hitec was 0.951 W/m.K, consistent with previously reported values for nitrate-nitrite salt systems[10,47,56–58]. For the HfB_2-containing samples, the conductivity increased to 1.289, 1.377, 1.507, and 1.689 W/m.K at 0.5, 1.0, 1.5, and 2.0 wt%, corresponding to enhancements of 35.54%, 44.79%, 58.46%, and 77.60%, respectively. For the SiB_6 series, the conductivity increased to 1.240, 1.359, 1.486, and 1.529 W/m.K at 0.5, 1.0, 1.5, and 2.0 wt%, corresponding to enhancements of 30.39%, 42.90%, 56.26%, and 60.78%, respectively. The increase in conductivity is attributed to conductive secondary-phase

pathways and reduced interparticle spacing, which facilitate heat propagation through the solidified matrix[59–62]. The departure from a perfectly linear trend is consistent with concentration-dependent dispersion quality and microstructural heterogeneity[17,63–65]. Local clustering can create densely connected particle-rich regions while leaving other regions less effectively connected, thereby moderating the macroscopic increment at higher loadings[17,66,67]. The thermal response should therefore be interpreted as a physical microstructural and interfacial effect, consistent with the FE-SEM observations and with previously reported heat-transport mechanisms in nano-enhanced thermal-storage materials[4,13,15,39,43,59,61,68]. Agglomeration at elevated loadings can restrict the development of a fully continuous network in both additive systems[39,69–71]. Direct comparison nevertheless shows that HfB_2 provides the stronger conductivity enhancement at every investigated loading, reaching 77.60% at 2.0 wt% compared with 60.78% for SiB_6. This stronger response is attributed to the material characteristics of HfB_2 together with increasing particle contacts and intergranular conductive pathways[17,39,72–74]. Since the XRD and FT-IR results reveal no new phase or bond formation, the conductivity improvement is interpreted as a physical microstructural effect rather than a consequence of chemical or phase transformation[43,59,61,68].

Specific heat capacity behaviour

The differential scanning calorimetry heat-flow curves of pristine Hitec and the nanocomposite salts over the 0–400 °C interval are presented in Fig. 12. These curves show how the thermal response evolves through the solid region, the phase-transition interval, and the fully molten state. Figure 13a-b gives the average C_p values determined separately for the solid and liquid phases, together with the associated y-error bars reflecting measurement scatter. Figure 13c-d shows the corresponding C_p enhancement percentages as a function of additive type and loading with respect to pristine Hitec. The relatively small error bars observed in these plots indicate good repeatability and suggest that the trends arise mainly from nanoadditive incorporation rather than experimental fluctuation. For pristine Hitec, the average C_p values were determined as 1.43612 J/g.°C in the solid phase and 1.51099 J/g.°C in the liquid phase. These values are consistent with the ranges commonly reported for pure Hitec salts, where solid-state specific heat capacity is generally around 1.40 J/g.°C and liquid-phase values are typically reported between 1.45 and 1.56 J/g·°C[3,8,47,75]. The agreement with literature indicates that the present measurements are reliable and that the prepared salt preserves the expected eutectic behavior. In addition, the weak secondary thermal signal near 100 °C in the differential scanning calorimetry curves may be associated with a solid-solid rearrangement separate from the principal phase transition or with other low-temperature thermal effects. A pronounced increase in thermal response through the melting interval further suggests that the supplied heat is consumed not only by temperature rise but also by disruption of the crystalline arrangement and by rearrangement of interfacial regions surrounding the nanoparticles[10,76]. This also explains why the C_p response becomes more sensitive to nanoadditive incorporation in the phase-transition region[8,39,77]. To quantify the influence of nanoparticle addition on specific heat capacity, the C_p enhancement percentage was calculated using Eq. 5[17]:

$$C_p\ enhancement\ (\%) = \left(\frac{C_{p,nano} - C_{p,Hitec}}{C_{p,Hitec}}\right) * 100 \quad (5)$$

In these expressions, $C_{p,\,nano}$ corresponds to the specific heat capacity of the nanocomposite formulations, whereas $C_{p,\,Hitec}$ refers to the same property for pristine Hitec in the corresponding phase. For the HfB_2-modified salts, the C_p values increase noticeably with additive loading and reach a maximum at approximately 1.5%. In the solid state, the C_p value at 0.5% HfB_2 is 1.47028 J/g.°C, corresponding to an increase of 2.38%. When the additive content is raised to 1%, the solid-phase C_p increases to 1.65689 J/g.°C, giving an improvement of 15.37%. At 1.5% loading, the solid-phase C_p reaches 2.22838 J/g.°C, which represents the maximum increase of 55.17%. When the HfB_2 content is further increased to 2%, the solid-phase C_p decreases to 1.98795 J/g.°C, although it still remains 38.43% higher than that of pristine Hitec. A comparable tendency is observed for the liquid phase. The

https://doi.org/10.1038/s41598-026-69109-x

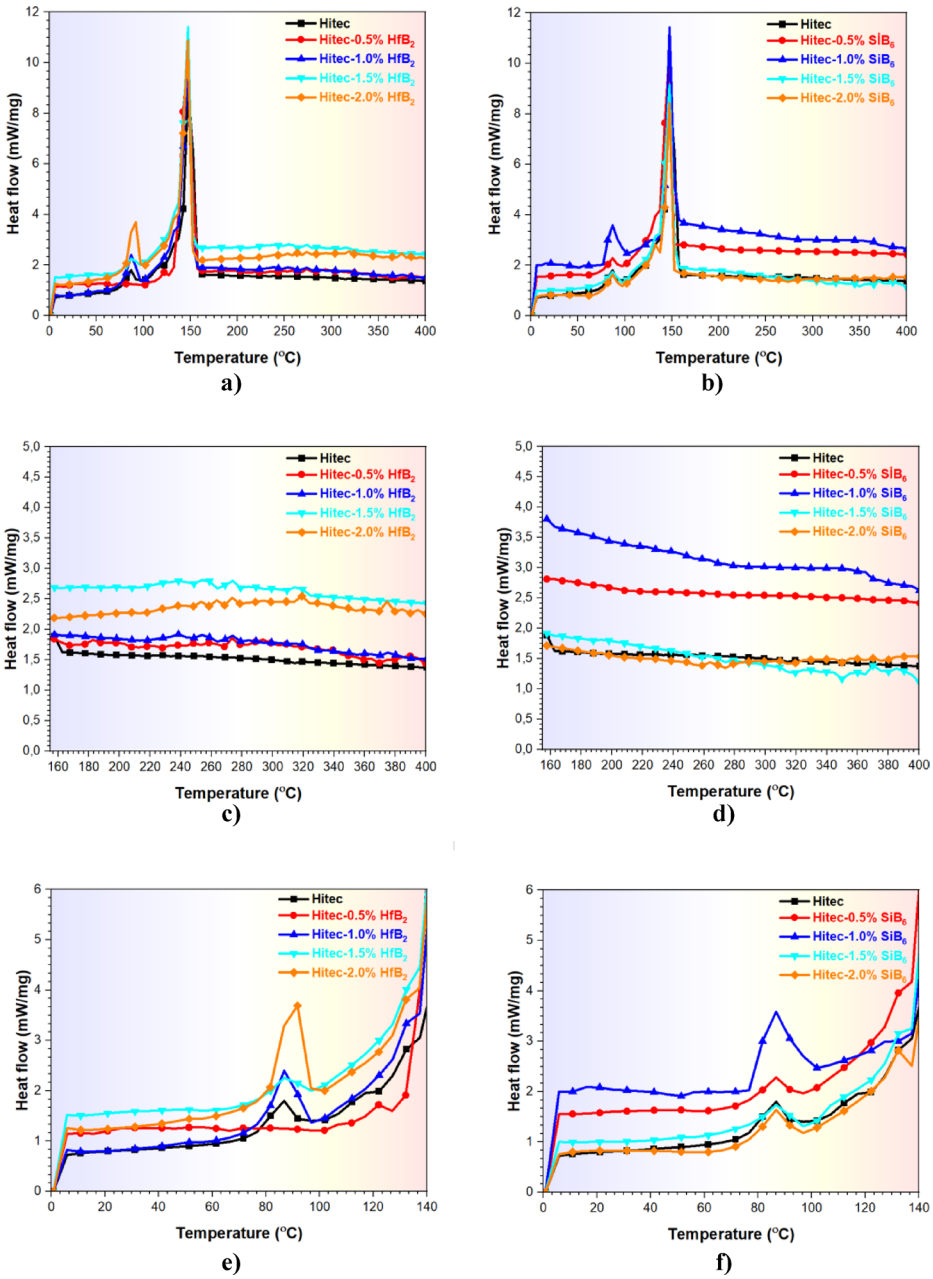


Fig. 12 C_p graph of (**a**, **c**, **e**) Hitec and HfB_2-added and (**b**, **d**, **f**) Hitec and SiB_6-added Hitec salts.

C_p enhancement values corresponding to 0.5%, 1%, 1.5%, and 2% HfB_2 additions are 11.22%, 21.60%, 66.65%, and 49.50%, respectively. These findings indicate that HfB_2 improves the energy storage capability of the salt in both phases, with the most effective performance occurring around 1.5% loading. The decrease observed at 2.0 wt% confirms that the C_p response is non-linear and identifies 1.5 wt% as the optimum HfB_2 loading under the present experimental conditions[3,4,13,39]. For the SiB_6-containing nanocomposite Hitec salts, the variation in C_p displays a more distinct optimum behavior. At 0.5% SiB_6, the solid-phase C_p reaches 2.27227 J/g.°C, corresponding to a 58.22% increase. Increasing the additive level to 1% further raises the C_p to 2.98397 J/g.°C, which represents the maximum enhancement of 107.78%. However, when the SiB_6 content is increased to 1.5% and 2%, the solid-phase C_p decreases to 1.50283 and 1.32640 J/g.°C, respectively. Under these conditions, the enhancement drops to 4.65% and becomes negative (− 7.64%) at 2%, indicating a value lower than that of pristine Hitec. A comparable evolution is also observed for the liquid phase, where high C_p enhancements of 70.45% and 117.79%

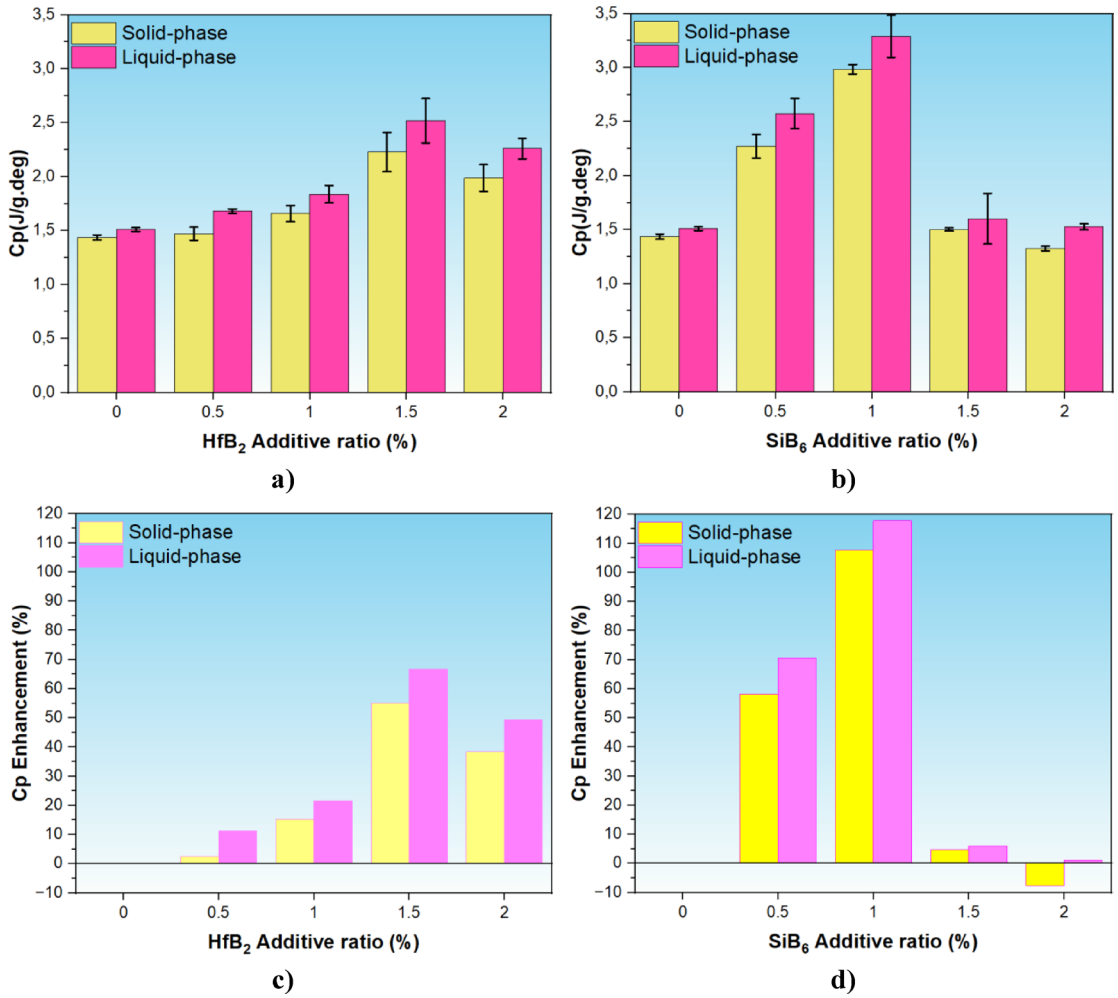


Fig. 13 Specific heat capacity (C_p) values of (**a**) pristine Hitec and HfB_2-containing Hitec salts and (**b**) pristine Hitec and SiB_6-containing Hitec salts, together with C_p enhancement values of (**c**) HfB_2-modified and (**d**) SiB_6-modified Hitec salts.

are obtained at 0.5% and 1% loadings, followed by a sharp reduction to 6.01% and 1.11% at higher concentrations. These observations indicate that the optimum additive content for the SiB_6-modified system is close to 1%, beyond which the beneficial contribution rapidly diminishes. Taken together, the C_p results identify 1.5 wt% HfB_2 and 1.0 wt% SiB_6 as the respective optimum loadings. The sharper decline in the SiB_6 series above 1.0 wt% and the more gradual decrease in the HfB_2 series indicate that the C_p response depends on additive-specific particle characteristics, accessible interfacial area, and concentration-dependent agglomeration[8,13,17,39,47]. This interpretation is consistent with the morphological observations of Sect. 3.1, in which additive-associated agglomerated regions are present in the compositions containing the highest additive contents. Interfacial rearrangement can enhance energy storage at suitable loadings, whereas clustering reduces the effective salt-particle contact available to contribute to C_p [4,13]. Therefore, C_p is governed by a balance between beneficial interfacial organization and agglomeration rather than by additive content alone.

Thermal stability behaviour

The thermogravimetric responses of pristine Hitec together with the HfB_2- and SiB_6-containing Hitec salts are compared in Fig. 14, which allows their degradation behavior to be evaluated under the same heating conditions. For pristine Hitec, the onset of thermal degradation was determined as 612 °C. This value is in reasonable

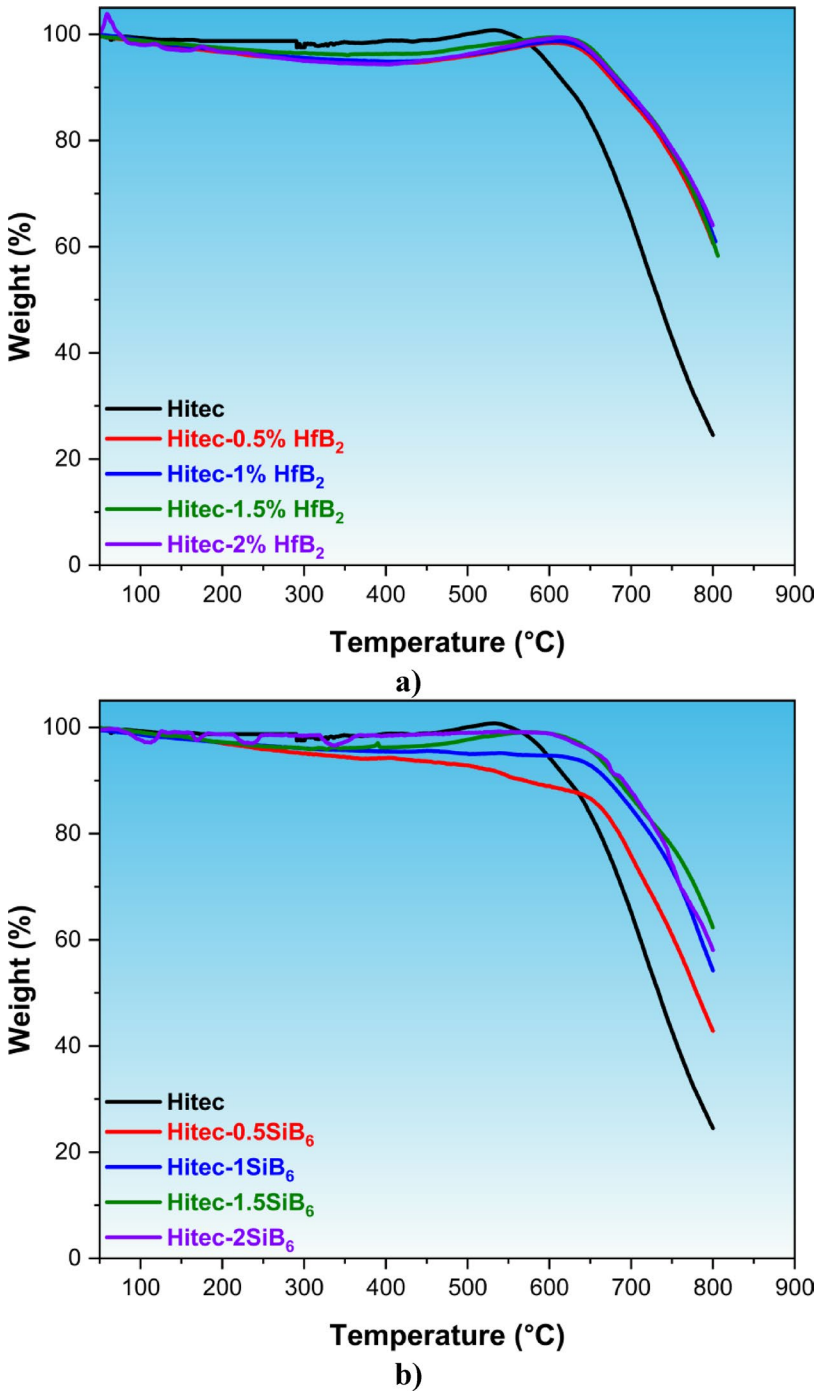


Fig. 14 Thermogravimetric analysis curves of pristine and nanoadditive-modified Hitec salts.

agreement with decomposition ranges commonly reported for Hitec-based molten salt systems, which are generally located in the low- to mid-600 °C region and often fall within approximately 630–650 °C. The close correspondence between the present result and previously published data indicates that the prepared reference salt exhibits the expected high-temperature behavior of Hitec and also supports the reliability and reproducibility of both the synthesis route and the thermogravimetric analysis procedure[5,8,13]. In this respect, the pristine salt provides a suitable baseline for evaluating the effect of nanoadditive incorporation. After HfB_2 addition, the degradation onset shifts toward higher temperatures, indicating improved thermal resistance. However, the magnitude of this improvement does not increase in a perfectly linear manner with additive content. Specifically, the onset

Table 3 Literature-based comparison of peak ΔH_{entm} enhancement, liquid-phase C_p improvement, and upper operating temperature increase in Hitec-based nanocomposite molten salts.

Ref.	Nanoparticle	Nanoparticle size	Maximum ΔH_{entm} enhancement (% / additive ratio)	C_p% max. at liquid-phase / additive ratio	Maximum upper working temperature enhancement (% / ditive ratio)
[5]	TiO_2	25 nm	78% / 0.1 wt%	5.5% / 0.1 wt%	5.2% / 0.1 wt%
[13]	CuO	≤ 50 nm	30% / 0.1 wt%	5.6% / 0.1 wt%	9.1% / 0.1 wt%
[8]	h-BN	70 nm	72% / 0.1 wt%	27% / 0.1 wt%	7% / 0.1 wt%
[4]	Al_2O_3	40–80 nm	–	5.77% / 2 wt%	–
[3]	Al_2O_3	< 50 nm	–	19.9% / 0.063 wt%	–
[10]	SiO_2	10–20 nm	–	15% / 1 wt%	–
[10]	Al_2O_3	< 50 nm	–	−43% / 1 wt%	–
[75]	Sn/SiO_x core-shell	Sn core 100 nm + SiO_x shell 10 nm	–	30% / 5 wt%	–
This work	HfB_2	50 nm	18.9% / 2 wt%	66.65% / 1.5 wt%	6.70% / 1.5 wt%
This work	SiB_6	40 nm	25.5% / 1 wt%	117.79% / 1 wt%	8.33% / 2 wt%

temperatures for Hitec salts containing 0.5%, 1%, 1.5%, and 2% HfB_2 were measured as 641 °C, 644 °C, 653 °C, and 648 °C, respectively. The pronounced enhancement observed at 1.5% HfB_2 suggests that this concentration provides the most effective stabilization within the investigated range. The slight decrease from 653 °C at 1.5 wt% to 648 °C at 2.0 wt% indicates that the HfB_2 stabilization effect reaches an optimum before higher-loading microstructural heterogeneity begins to limit the response[39,78,79]. A more gradual and sustained stabilization behavior is observed for the SiB_6 nanoadditive Hitec salts. In this case, the degradation onset temperature increases progressively with additive concentration, reaching 652 °C, 655 °C, 657 °C, and 663 °C for 0.5%, 1%, 1.5%, and 2% SiB_6 nanoadditions, respectively. The continuous upward shift indicates that SiB_6 remains effective in delaying degradation processes across the entire concentration range investigated, without exhibiting the saturation or reversal behavior noted for HfB_2. The highest onset temperature of 663 °C achieved at 2% SiB_6 represents the maximum thermal stabilization among all compositions examined in this study. The upward shifts in degradation onset are attributed to the thermal robustness of the boride inclusions and their concentration-dependent physical distribution within the Hitec matrix[39,43,49,78,79]. The HfB_2 series reaches its optimum at 1.5 wt% and then declines slightly, whereas SiB_6 produces a progressive increase up to 663 °C at 2.0 wt%. This additive-specific behaviour is consistent with the differing microstructural distributions observed in Sect. 3.1. Since the XRD and FT-IR results show preservation of the Hitec phase and bonding framework, the improvement is interpreted as physical microstructural stabilization rather than chemical transformation. Overall, SiB_6 provides the highest degradation onset temperature, while HfB_2 provides its strongest stabilization at 1.5 wt%.

As summarized in Table 3, earlier studies on Hitec molten salt systems have mainly concentrated on oxide nanoparticles and layered additives, typically applied at very low contents around 0.1 wt%[5,8,13]. In such systems, very high melting enthalpy improvements have been reported, reaching up to 78% for TiO_2[5] and 72% for h-BN[8]. However, these large ΔH_{entm} increases are usually confined to a narrow concentration range and tend to decrease rapidly once the additive level exceeds the optimum. This behavior indicates a strong dependence on dispersion conditions and limits the practical applicability of oxide- and layered-additive systems under broader processing conditions. In contrast, the present results show that boride-based ceramic nanoadditives provide a more balanced improvement across multiple thermophysical properties. Although the maximum ΔH_{entm} enhancements obtained with HfB_2 (18.9% at 2 wt%) and SiB_6 (25.5% at 1 wt%) are lower than the peak values reported for TiO_2 and h-BN at 0.1 wt%[5,8], these improvements are achieved at considerably higher additive loadings, offering greater flexibility in practical applications. This distinction indicates that boride-based systems can tolerate a wider concentration range without abrupt performance degradation, which is a key advantage for scale-up and long-term operation. A key contribution of the present study is the magnitude of the specific heat capacity improvement, particularly in the SiB_6-modified Hitec salt. The maximum liquid-phase C_p enhancement reaches 117.79% at 1 wt% SiB_6, exceeding the values reported for many oxide-based additives and layered systems, including

Al_2O_3[3,4,10], SiO_2[10], and h-BN[8]. The HfB_2-containing system also shows a substantial liquid-phase C_p increase of 66.65% at 1.5 wt%, placing it among the stronger-performing Hitec-based nanocomposite systems reported in the literature to date. These findings indicate that boride-based nanoadditives can provide highly competitive specific heat capacity enhancement while maintaining the structural and chemical stability of the salt matrix. With respect to thermal stability, the upper working temperature enhancements achieved in the present study are comparable to or exceed those reported for several oxide-based systems. While TiO_2, CuO, and h-BN-added Hitec salts typically exhibit upper working temperature improvements in the range of 5–9% at low loadings[5,8,13], the SiB_6-added Hitec salt achieves an enhancement of 8.33% at 2 wt%, and the HfB_2 system reaches 6.70% at 1.5 wt%. Importantly, these gains are obtained concurrently with strong enhancements in both ΔH_{entm} and C_p whereas many literature studies report improvements in one parameter at the expense of others. Despite these advantages, ΔH_{entm} and C_p remain concentration-dependent, particularly in the SiB_6 series, and therefore require careful optimization of additive loading[3,10]. Taken together, the comparison of literature indicates that the key advantage of the present work does not lie in maximizing a single thermophysical parameter at minimal loading, but rather in achieving a robust and simultaneous enhancement of melting enthalpy, specific heat capacity, and upper working temperature within a chemically and structurally stable framework. While oxide-based additives can yield very high ΔH_{entm} enhancements at ultra-low concentrations[5,8], the boride-based HfB_2 and SiB_6 nanoadditives introduced in this study offer a favorable balance between performance magnitude, concentration tolerance, and multi-property enhancement, with SiB_6 exhibiting stronger C_p, latent heat, and upper-temperature improvements, while HfB_2 delivers the strongest thermal conductivity enhancement. Overall, SiB_6 provides the strongest combined improvements in phase-change energetics, C_p, and thermal stability, whereas HfB_2 provides the highest thermal-conductivity enhancement. The increase in ΔT should therefore be evaluated together with these simultaneous gains rather than as an isolated performance metric. The combined performance improvements obtained in this study have important implications for concentrating solar power systems and other high-temperature thermal energy storage applications in which molten salt functions simultaneously as the heat-transfer fluid and the storage medium. The increase in ΔHentm corresponds to a higher phase-change energy density, which can lower the storage mass or volume required to achieve a given latent-heat capacity and can also improve heat recovery during melting and solidification. In particular, the very large liquid-phase C_p enhancement obtained with SiB_6 provides a clear benefit for sensible-heat storage by increasing the stored energy per unit mass per degree, thereby supporting more compact storage-tank designs at the same thermal capacity. In addition, the higher upper operating temperature observed in the boride-modified systems broadens the usable temperature range of Hitec, enabling safer operation at elevated temperatures and improving compatibility with advanced concentrating solar power cycles. When these effects are considered together with the thermal conductivity improvements demonstrated in this work, the results indicate that both HfB_2 and SiB_6-modified Hitec salts are promising materials for next-generation concentrating solar power-based thermal energy storage and heat-transfer applications, with HfB_2 being especially attractive when rapid heat transfer is prioritized and SiB_6 being particularly advantageous when maximizing heat-storage capacity and thermal stability. Although nanoparticle incorporation leads to an increase in supercooling, the phase-change temperature interval remains close to that of pristine Hitec, and the associated penalty remains manageable in view of the substantial gains in energy density, heat-transfer capability, and thermal robustness. Despite the strong performance gains, several limitations should be acknowledged. First, the non-linear concentration dependence, particularly in the SiB_6 series, requires careful optimization of additive content and dispersion conditions. Second, while the present study establishes clear improvements in key metrics, long-term thermal cycling stability under extended operating durations and realistic CSP conditions has not been fully addressed and warrants further investigation. Third, system-level factors such as viscosity variation, pumping power penalties, and corrosion behavior in contact with typical receiver and piping alloys should be examined in future work to evaluate full-scale applicability. Addressing these aspects through long-duration cycling tests and integrated system evaluations will be essential to translate the demonstrated boride-based nanoenhancement strategy into practical high-temperature energy storage deployments.

Conclusions

In this study, Hitec molten salt was enhanced with HfB_2 and SiB_6 nanoparticles to address the key performance requirements for heat transfer and thermal energy storage in CSP systems, including higher storage capacity, faster heat transfer, safe high-temperature operation, and preservation of material integrity. Structural and morphological evaluations confirmed that the fundamental nitrate–nitrite character of the Hitec matrix was maintained, no new phases or chemical bonds were formed, and the nanoparticles were physically integrated into the molten salt. Therefore, the observed performance enhancements were attributed to microstructural and interfacial effects rather than chemical transformation through phase evolution.

- The maximum melting enthalpy reached 95.6 J/g in the Hitec–1.0 wt% SiB_6 composition, indicating a significant increase in thermal energy storage density.
- The highest solidification enthalpy of 97.3 J/g was obtained for Hitec 0.5 wt% SiB_6, supporting improved energy recovery during thermal cycling.
- The maximum melting mass fraction enhancement reached 125.5% in Hitec 1 wt% SiB_6, while the highest solidification mass fraction enhancement of 135.9% was observed in Hitec 0.5 wt% SiB_6, indicating more effective phase change utilization.
- The phase-transition temperatures were retained within a limited operating interval. For pristine Hitec, the onset and peak melting temperatures were 138.6 °C and 144.6 °C, respectively, indicating that the improved performance was achieved without significantly altering the usable temperature range.
- The supercooling degree rose from 4.3 °C for pristine Hitec to 12.1 °C at 1 wt% HfB_2 and 10.8 °C at 1 wt% SiB_6. Despite this change, the increase can be considered moderate in relation to the overall performance improvements, as the phase-transition range remained essentially unchanged while notable enhancements in energy storage capacity, heat transfer, and thermal stability were maintained.
- The strongest enhancement in specific heat capacity was achieved for Hitec 1 wt% SiB_6, with a 107.78% increase in the solid phase corresponding to a C_p of 2.98397 J/g.°C, and a 117.79% increase in the liquid phase.
- For HfB_2, the optimum specific heat capacity response occurred at 1.5 wt%, where the specific heat capacity reached 2.22838 J/g.°C, corresponding to 55.17% and 66.65% increases in the solid and liquid states, respectively.
- The highest thermal conductivity achieved with HfB_2 addition was 1.689 W/m.K in Hitec 2 wt% HfB_2, corresponding to a 77.60% increase.
- In the SiB_6 series, the thermal conductivity increased to a maximum of 1.529 W/m.K in Hitec 2 wt% SiB_6, representing a 60.78% enhancement in heat-transfer capability.
- Thermal stability improved markedly, with the degradation onset showing a maximum increase of 8.33% in the 2 wt% SiB_6 composition and 6.70% in the 1.5 wt% HfB_2 composition.

From an application standpoint, these improvements directly target key limitations of concentrated solar power-based thermal energy systems. The marked increases in melting enthalpy and specific heat capacity translate into higher energy storage density, making it possible to achieve the same energy output with more compact storage units and lower material demand. The increase in thermal conductivity also promotes faster heat exchange, lowers thermal resistance, and shortens charge-discharge times in heat-transfer circuits and heat exchangers. In addition, the higher degradation onset temperature broadens the safe operating interval of Hitec molten salt, enabling more reliable use at elevated temperatures and contributing to improved overall system performance. Taken together, these findings show that both HfB_2 and SiB_6 nanoparticle incorporation provide highly effective routes for advancing Hitec molten salt as a multifunctional medium for both heat transfer and thermal energy storage in next-generation concentrated solar power applications. HfB_2 is especially beneficial for maximizing thermal conductivity, whereas SiB_6 offers the strongest combined gains in latent heat, specific heat capacity, and thermal stability.

Acknowledgements This study was supported by the Scientific and Technological Research Council of Türkiye (TÜBİTAK) under the project number 223M467. The authors gratefully acknowledge the financial support provided by TÜBİTAK within the scope of this project. The authors would like to acknowledge that part of the outcomes of this research have been submitted as a patent application (Turkish Patent Application No: TR2024015453A2). The authors would like to thank the Firat University Scientific Research Projects Coordination Unit for supporting this research under Project No: FUBAP-TEKF.26.20. The authors also acknowledge the support provided for the open access publication process of this study. During the preparation of this manuscript, OpenAI's ChatGPT (GPT-5.5, 2026 release) was used to improve the readability of selected sections and correct language errors. All generated content was carefully reviewed and edited by the authors, and the authors take full responsibility for the final published version of the manuscript.

Author contributions E. G.: Writing – review & editing, Writing – original draft, Methodology, Investigation, Formal analysis, Funding acquisition, Project administration, Conceptualization. H. İ. Y.: Writing – review & editing, Writing – original draft, Methodology, Formal analysis, Conceptualization. M. Ö.: Writing – original draft, Formal analysis, Conceptualization. Canan Aksu Canbay: Writing – review & editing, Methodology, Formal analysis. T. G.: Writing – review & editing, Supervision, Conceptualization. M. G.: Writing – original draft, Conceptualization. H. F. Ö.: Writing – review & editing, Writing – original draft, Supervision, Methodology. E. S. S.: Writing – original draft, Conceptualization, Investigation.

Funding This study was supported by the Scientific and Technological Research Council of Türkiye (TÜBİTAK) under the project number 223M467. The authors would like to thank the Firat University Scientific Research Projects Coordination Unit for supporting this research under Project No: FUBAP-TEKF.26.20.

Data availability The experimental data, characterization results, and thermophysical measurement datasets generated and analyzed during this study are available from the corresponding author upon reasonable request.

Declarations

Competing interests The authors declare no competing interests.

Consent for publication All authors have approved the final version of the manuscript and consented to its submission for publication.

Open Access This article is licensed under a Creative Commons Attribution-NonCommercial-NoDerivatives 4.0 International License, which permits any non-commercial use, sharing, distribution and reproduction in any medium or format, as long as you give appropriate credit to the original author(s) and the source, provide a link to the Creative Commons licence, and indicate if you modified the licensed material. You do not have permission under this licence to share adapted material derived from this article or parts of it. The images or other third party material in this article are included in the article's Creative Commons licence, unless indicated otherwise in a credit line to the material. If material is not included in the article's Creative Commons licence and your intended use is not permitted by statutory regulation or exceeds the permitted use, you will need to obtain permission directly from the copyright holder. To view a copy of this licence, visit http://creativecommons.org/licenses/by-nc-nd/4.0/.

References

1. Ho, M. X. & Pan, C. Experimental investigation of heat transfer performance of molten HITEC salt flow with alumina nanoparticles. *Int. J. Heat. Mass. Transf.* **107**, 1094–1103 (2017).
2. Zhang, Z. & Chen, M. Molecular insights into synergistic enhancement of thermal conductivity and thermal energy storage performance in molten salt-based nanofluids. *Mater. Today Commun.* **48**, 113324 (2025).
3. Ho, M. X. & Pan, C. Optimal concentration of alumina nanoparticles in molten hitec salt to maximize its specific heat capacity. *Int. J. Heat. Mass. Transf.* **70**, 174–184 (2014).
4. Xiao, X., Jia, H., Wen, D. & Zhao, X. Thermal performance analysis of a solar energy storage unit encapsulated with HITEC salt/copper foam/nanoparticles composite. *Energy* **192**, 116593 (2020).
5. Aljaerani, H. A. et al. Effect of TiO2 nanoparticles on the thermal energy storage of HITEC salt for concentrated solar power applications. *J. Energy Storage*. **72**, 108449 (2023).
6. Isaza-Ruiz, M., Mondragón, R., Bolívar Osorio, F., Ventura-Espinosa, J. & Hernández, L. Viscosity and stability analysis of hitec salt-based alumina nanofluids. *Sol Energy Mater. Sol Cells*. **222**, 110923 (2021).

7. Xu, Q., Wang, S., Luo, K. & Fan, J. Optimization of design and performance for a heat storage system using molten salt coupled with a supercritical coal-fired power plant. *Therm. Sci. Eng. Prog*. **68**, 104283 (2025).
8. Suraparaju, S. K. et al. Thermal properties analysis and thermal cycling of HITEC molten salt with h-BN nanoparticles for CSP thermal energy storage applications. *Environ. Sci. Pollut Res.* **31**, 50166–50178 (2024).
9. Dong, S., Zhang, M., Jin, K. & Yang, R. An improved laser flash method for thermal conductivity measurement of molten salts. *Prog Nat. Sci. Mater. Int.* **34**, 345–353 (2024).
10. Parida, D. R. & Basu, S. On the specific heat capacity of HITEC-salt nanocomposites for concentrated solar power applications. *RSC Adv.* **13**, 5496–5508 (2023).
11. Hu, Z. et al. Corrosion behavior and mechanism of 316 stainless steel in NaCl-KCl-ZnCl2 molten salts at high temperature. *Mater. Today Commun.* **31**, 103297 (2022).
12. Nunes, V. M. B., Queirós, C. S., Lourenço, M. J. V. & Santos, F. J. V. Nieto de Castro, C. A. Molten salts as engineering fluids – A review: Part I. Molten alkali nitrates. *Appl. Energy*. **183**, 603–611 (2016).
13. Aljaerani, H. A. et al. Thermophysical properties enhancement and characterization of CuO nanoparticles enhanced HITEC molten salt for concentrated solar power applications. *Int. Commun. Heat. Mass. Transf.* **132**, 105898 (2022).
14. Gao, Y. et al. Solid-liquid phase change materials microcapsules: Synthesis strategies, thermal storage and beyond. *Prog Nat. Sci. Mater. Int.* **34**, 615–631 (2024).
15. Gurgenc, E. et al. B4C-based nanoenhancement on the thermophysical and stability performance of solar salt: a novel approach for high-temperature TES applications. *Case Stud. Therm. Eng.* **75**, 107257 (2025).
16. Enemuo, M., Enemuo, N., Taleghani, A. D. & Ogunmodimu, O. Slags as Thermal Energy Storage Media for Concentrated Solar Power and Renewable Energy Integration. *Energy Storage*. **7**, 70274 (2025).
17. Gurgenc, E. et al. Novel boride-enhanced solar salts: Thermophysical and structural properties for thermal energy storage. *J. Energy Storage*. **143**, 119207 (2026).
18. Hu, M. et al. The role of H2O in the corrosion of SiC in the vapor of molten NaCl-KCl-MgCl2 salt in a 316L SS container. *Mater. Today Commun.* **41**, 110865 (2024).
19. Zoli, L., Sciti, D. & Sani, E. Zirconium diboride-based nanofluids for solar energy applications. *J. Mol. Liq*. **322**, 114981 (2021).
20. Nekahi, S. et al. A numerical approach to the heat transfer and thermal stress in a gas turbine stator blade made of HfB2. *Ceram. Int.* **45**, 24060–24069 (2019).
21. Zou, Z., Qin, Y., Chang, K. & Huang, Z. Thermal properties and oxidative corrosion behaviour of HfB2-SiB6 ceramicizable phenolic resin matrix composites. *Corros. Sci.* **221**, 111340 (2023).
22. Zou, Z. et al. Thermal properties, oxidation corrosion behavior, and the in situ ceramization mechanism of SiB6@BPR/HF composites under high-temperature corrosion. *Corros. Sci.* **193**, 109913 (2021).
23. Gurgenc, E. et al. Performance enhancement of Hitec molten salt through TiB2 and ZrB2 nanoadditives for High-Temperature TES and CSP applications. *Sol Energy Mater. Sol Cells*. **301**, 114298 (2026).
24. Gurgenc, E. et al. Interfacial and thermophysical engineering for enhanced thermal performance of boron carbide-modified HITEC nanocomposites in high-temperature thermal energy storage applications. *J. Mater. Res. Technol.* **42**, 1589–1612 (2026).
25. Khajavinia, A. & El-Aneed, A. Carbon-Based Nanoparticles and Their Surface-Modified Counterparts as MALDI Matrices. *Anal. Chem.* **95**, 100–114 (2023).
26. Wang, T. et al. Dispersant-assisted preparation of ultra-fine HfB2 powder. *Appl. Surf. Sci.* **606**, 154995 (2022).
27. Zhang, J., Xiong, S., Wang, J., Ni, Y. & Ke, C. Silicothermic synthesis of phase-pure HfB2 fine powder. *J. Am. Ceram. Soc.* **104**, 785–792 (2021).
28. Imam, M. A., Young, J. S. & Reddy, R. G. Effect of Oxygen Partial Pressure and Temperature on the Oxidation Behavior of SiB6. *Metall. Mater. Trans. B Process. Metall. Mater. Process. Sci.* **51**, 386–394 (2020).
29. Arshad, A. et al. Development of TiO2/RT–35HC based nanocomposite phase change materials (NCPCMs) for thermal management applications. *Sustain. Energy Technol. Assessments*. **43**, 100865 (2021).
30. Arshad, A., Jabbal, M. & Yan, Y. Thermophysical characteristics and application of metallic-oxide based mono and hybrid nanocomposite phase change materials for thermal management systems. *Appl. Therm. Eng.* **181**, 115999 (2020).
31. Orozco, M. A., Acurio, K., Vásquez-Aza, F., Martínez-Gómez, J. & Chico-Proano, A. Thermal storage of nitrate salts as phase change materials (PCMs). *Mater. (Basel)*. **14**, 7223 (2021).
32. Fernández, A. G., Galleguillos, H., Fuentealba, E. & Pérez, F. J. Thermal characterization of HITEC molten salt for energy storage in solar linear concentrated technology. *J. Therm. Anal. Calorim.* **122**, 3–9 (2015).
33. Li, J., Zhang, Y., Zhao, Y., Wang, M. & Yang, Y. Novel high specific heat capacity ternary nitrate/nitrite eutectic salt for solar thermal energy storage. *Sol Energy Mater. Sol Cells*. **227**, 111075 (2021).
34. Dunlop, T. O., Jarvis, D. J., Voice, W. E. & Sullivan, J. H. Stabilization of molten salt materials using metal chlorides for solar thermal storage. *Sci. Rep.* **8**, 8190 (2018).
35. Yan, C. et al. BN white graphene well-dispersed solar salt nanofluids with significant improved thermal properties for concentrated solar power plants. *Sol Energy Mater. Sol Cells*. **245**, 111875 (2022).

36. Abir, F. M., Altwarah, Q., Rana, M. T. & Shin, D. Recent Advances in Molten Salt-Based Nanofluids as Thermal Energy Storage in Concentrated Solar Power: A Comprehensive Review. *Mater. (Basel)*. **17**, 955 (2024).
37. Deng, Q. et al. Mediating dielectric/breakdown conflict in polydopamine@HfB2 nanorod-filled polymer composites from rational meaty-sandwich structure. *J. Mater. Sci. Mater. Electron.* **30**, 21305–21315 (2019).
38. Lozanov, V. V. et al. New hard ternary Hf–Ir–B borides formed by reaction hafnium diboride with iridium. *J. Am. Ceram. Soc.* **105**, 2323–2333 (2022).
39. Pradeep, N., Nithiyanantham, U. & Reddy, K. S. Impact on thermophysical properties of solar salt with different concentrations of SiC nanoparticles for thermal energy storage system. *Sol Energy Mater. Sol Cells*. **277**, 113130 (2024).
40. Öztop, H. F., Gürgenç, E. & Gür, M. Thermophysical properties and enhancement behavior of novel B4C-nanoadditive RT35HC nanocomposite phase change materials: Structural, morphological, thermal energy storage and thermal stability. *Sol Energy Mater. Sol Cells*. **272**, 112909 (2024).
41. Zhang, H., Du, S., Wang, Y. & Xue, F. Prevention of Crystal Agglomeration: Mechanisms, Factors, and Impact of Additives. *Crystals* **14**, 676 (2024).
42. Li, L. et al. Graphene as a heat transfer enhancer for ternary molten salt applications. *Sci. Rep.* **16**, 1437 (2026).
43. Saranprabhu, M. K. & Rajan, K. S. Magnesium oxide nanoparticles dispersed solar salt with improved solid phase thermal conductivity and specific heat for latent heat thermal energy storage. *Renew. Energy*. **141**, 451–459 (2019).
44. Baris, M., Simsek, T., Simsek, T., Ozcan, S. & Kalkan, B. High purity synthesis of ZrB2 by a combined ball milling and carbothermal method: Structural and magnetic properties. *Adv. Powder Technol.* **29**, 2440–2446 (2018).
45. Lasfargues, M., Bell, A. & Ding, Y. In situ production of titanium dioxide nanoparticles in molten salt phase for thermal energy storage and heat-transfer fluid applications. *J. Nanoparticle Res.* **18**, 150 (2016).
46. Bauer, T., Laing, D. & Tamme, R. Recent Progress in Alkali Nitrate/Nitrite Developments for Solar Thermal Power Applications. *Molten Salts Chem. Technol.* **9781118448**, 543–553 (2014).
47. Zhang, H. et al. Study on thermophysical properties of porous aluminosilicate ceramics/hitec melting salt composite phase change material: A thermal storage application. *Sol Energy*. **299**, 113742 (2025).
48. Mondragón, R., Juliá, J. E., Cabedo, L. & Navarrete, N. On the relationship between the specific heat enhancement of salt-based nanofluids and the ionic exchange capacity of nanoparticles. *Sci. Rep.* **8**, 7532 (2018).
49. Fernández, A. G., Muñoz-Sánchez, B. & Nieto-Maestre, J. García-Romero, A. High temperature corrosion behavior on molten nitrate salt-based nanofluids for CSP plants. *Renew. Energy*. **130**, 902–909 (2019).
50. Beaupere, N., Soupremanien, U. & Zalewski, L. Nucleation triggering methods in supercooled phase change materials (PCM), a review. *Thermochim Acta*. **670**, 184–201 (2018).
51. Fernández, A. G. & Pérez, F. J. Improvement of the corrosion properties in ternary molten nitrate salts for direct energy storage in CSP plants. *Sol Energy*. **134**, 468–478 (2016).
52. Chen, J., Ling, Z., Fang, X., Wu, Y. & Zhang, Z. Numerical simulation on the flow and heat transfer characteristics of molten salt nanofluid in the shell-side of helical baffle heat exchangers with elliptic tubes and circular tubes. *Sol Energy Mater. Sol Cells*. **290**, 113733 (2025).
53. Tian, H. et al. Enhanced thermal conductivity of ternary carbonate salt phase change material with Mg particles for solar thermal energy storage. *Appl. Energy*. **204**, 525–530 (2017).
54. Zhang, G. et al. Preparation and control mechanism of nano-phase change emulsion with high thermal conductivity and low supercooling for thermal energy storage. *Energy Rep.* **8**, 8301–8311 (2022).
55. Mishra, A. K., Lahiri, B. B. & Philip, J. Effect of Surface Functionalization and Physical Properties of Nanoinclusions on Thermal Conductivity Enhancement in an Organic Phase Change Material. *ACS Omega*. **3**, 9487–9504 (2018).
56. Isaza-Ruiz, M. & Osorio, F. B. Thermal Properties Of Hitec Salt-Based Nanofluids Synthesized By New Two-Step Method. *Procedia Environ. Sci. Eng. Manag*. **8**, 147–155 (2021).
57. Muhmood, L. Modeling for Thermal Conductivity of Ternary Molten Nitrate Salts Using Unit Cell Concept. *Int. J. Thermophys.* **41**, 127 (2020).
58. Li, N., Wang, Y., Liu, Q. & Peng, H. Evaluation of Thermal-Physical Properties of Novel Multicomponent Molten Nitrate Salts for Heat Transfer and Storage. *Energies* **15**, 6591 (2022).
59. Li, Q. et al. Mechanical, electrical and thermal properties of HfC-HfB2-SiC ternary eutectic composites prepared by arc melting. *J. Eur. Ceram. Soc.* **41**, 6943–6951 (2021).
60. Zhang, P. et al. A Theoretical Review on Interfacial Thermal Transport at the Nanoscale. *Small* **14**, 1702769 (2018).
61. Fang, M., Cao, L., Cao, Y. & Hou, F. Enhanced thermal energy storage in molten salt-based date-occupied composites with SiO2 nanoparticles. *Appl. Therm. Eng.* **270**, 126209 (2025).
62. Meng, L. et al. Study on thermophysical properties improvement of ternary nitrate-carbonate molten salt by adding SiO2 nanoparticles for large-scale thermal energy storage. *Sol Energy Mater. Sol Cells*. **292**, 113819 (2025).
63. Timofeeva, E. V. et al. Thermal conductivity and particle agglomeration in alumina nanofluids: Experiment and theory. *Phys. Rev. E - Stat. Nonlinear Soft Matter Phys.* **76**, 061203 (2007).
64. Coetzee, D., Venkataraman, M., Militky, J. & Petru, M. Influence of nanoparticles on thermal and electrical conductivity of composites. *Polym. (Basel)*. **12**, 742 (2020).

65. Rao, Z., Bai, R., Ye, K. & Zhou, T. Effects of interfacial layer on thermal conductivity enhancement of solar salt-based nanofluids: Insights from molecular dynamics simulations. *Case Stud. Therm. Eng.* **35**, 102087 (2022).
66. Jo, B. & Banerjee, D. Enhanced specific heat capacity of molten salt-based nanomaterials: Effects of nanoparticle dispersion and solvent material. *Acta Mater.* **75**, 80–91 (2014).
67. Peng, Q., Ding, J., Wei, X., Yang, J. & Yang, X. The preparation and properties of multi-component molten salts. *Appl. Energy*. **87**, 2812–2817 (2010).
68. Cockrell, C. et al. Thermal Conductivity and Thermal Diffusivity of Molten Salts: Insights from Molecular Dynamics Simulations and Fundamental Bounds. *J. Phys. Chem. B*. **129**, 2271–2279 (2025).
69. Nithiyanantham, U., Pradeep, N. & Reddy, K. S. Development and comparison of multi-walled carbon nanotubes and graphite nanoflakes dispersed solar salt: Structural formation and thermophysical properties. *J. Mol. Liq*. **402**, 124787 (2024).
70. Gautam, S., Verma, M., Chauhan, R. & Aghara, S. Goyal, N. Reviewing thermal conductivity aspects of solar salt energy storage. *Energy Adv.* **2**, 1309–1325 (2023).
71. Sun, X., Liu, L., Mo, Y., Li, J. & Li, C. Enhanced thermal energy storage of a paraffin-based phase change material (PCM) using nano carbons. *Appl. Therm. Eng.* **181**, 115992 (2020).
72. Arshad, A., Jabbal, M. & Yan, Y. Preparation and characteristics evaluation of mono and hybrid nano-enhanced phase change materials (NePCMs) for thermal management of microelectronics. *Energy Convers. Manag*. **205**, 112444 (2020).
73. Bhatnagar, P., Siddiqui, S., Sreedhar, I. & Parameshwaran, R. Molten salts: Potential candidates for thermal energy storage applications. *Int. J. Energy Res.* **46**, 17755–17785 (2022).
74. Kalidasan, B., Pandey, A. K., Saidur, R., Samykano, M. & Tyagi, V. V. Nano additive enhanced salt hydrate phase change materials for thermal energy storage. *Int. Mater. Rev.* **68**, 140–183 (2023).
75. Lai, C. C. et al. A solar-thermal energy harvesting scheme: Enhanced heat capacity of molten HITEC salt mixed with Sn/SiOx core-shell nanoparticles. *Nanoscale* **6**, 4555–4559 (2014).
76. Zhang, P., Cheng, J., Jin, Y. & An, X. Evaluation of thermal physical properties of molten nitrate salts with low melting temperature. *Sol Energy Mater. Sol Cells*. **176**, 36–41 (2018).
77. Upadhyay, V. V., Singhal, S. & Pandey, A. Thermal performance and characterization of phase change material composites reinforced with nano-particles in thermal energy storage systems: a review. *Eng. Res. Express*. **6**, 042503 (2024).
78. Nithiyanantham, U. et al. Shape effect of Al2O3 nanoparticles on the thermophysical properties and viscosity of molten salt nanofluids for TES application at CSP plants. *Appl. Therm. Eng.* **169**, 114942 (2020).
79. Popov, O., Avramenko, T. & Vishnyakov, V. Thermal conductivity and thermal shock resistance of TiB2-basedUHTCs enhanced by graphite platelets. *Mater. Today Commun.* **26**, 101756 (2021).

Publisher's note Springer Nature remains neutral with regard to jurisdictional claims in published maps and institutional affiliations.

Authors and Affiliations

Ezgi Gurgenc[1] · Halil İbrahim Yamaç[2] · Murat Özabacı[3] · Canan Aksu Canbay[4] · Turan Gurgenc[5] · Muhammed Gür[1] · Hakan F. Öztop[1,6,7] · Elshan Sefidgar Shahanaghi[5]

✉ Halil İbrahim Yamaç
hiyamac@firat.edu.tr

[1] Department of Mechanical Engineering, Technology Faculty, Firat University, Elazig 23119, Turkey

[2] Department of Mechatronics Engineering, Technology Faculty, Firat University, Elazig 23119, Turkey

[3] Scientific and Technological Research Center, Inonu University, Malatya, Turkey

[4] Department of Physics, Faculty of Science, Firat University, Elazig 23119, Turkey

[5] Department of Automotive Engineering, Technology Faculty, Firat University, Elazig 23119, Turkey

[6] Faculty of Engineering and Natural Sciences, Istinye University, 34396 Istanbul, Turkey

[7] Department of Medical Research, China Medical University Hospital, China Medical University, Taichung, Taiwan